LITHOS 544–545 (2026) 108742

Contents lists available at ScienceDirect

LITHOS

journal homepage: www.elsevier.com/locate/lithos

From ultra-depleted harzburgite to refertilized lherzolite: Multi-stage metasomatism and crustal recycling recorded by garnet populations from the Newlands Kimberlite, South Africa

C. Bonadiman [a,*], L. Milani [b], R. Tassinari [a], N. Lenhardt [b], P.W.J. Delport [b], L. Rowe [b]

[a] Department of Physics and Earth Sciences, University of Ferrara, Italy
[b] Department of Geology, University of Pretoria, Private Bag X20, Hatfield 0028, South Africa

ARTICLE INFO

Keywords:
Kaapvaal Craton
Ultra-depleted Cr-pyrope
Cr-Ca-rich garnet
Mantle metasomatism

ABSTRACT

This study investigates the diamondiferous Newlands kimberlite (South Africa, ~144 Ma), a Group II orangeite characterized by a prolific variety of garnet xenocrysts despite a scarcity of intact mantle xenoliths. By analyzing the geochemical signatures of Cr-pyrope populations, this study reconstructs the dynamic evolution and stratified nature of the Kaapvaal lithospheric mantle.

The deepest section (~ 5.0 GPa; 145–155 km) is represented by Cr-pyrope type 4, which exhibits ultra-depleted CaO and trace-element profiles consistent with high-pressure exsolution from residual orthopyroxene. These garnets testify to a highly depleted harzburgitic mantle at the incipient stages of metasomatism, providing a redox-favourable environment for diamond stability. In contrast, Cr-pyropes type 3 and 2 record a progressive transition towards a more oxidized, lherzolitic composition. This evolution is driven by continuous melt-rock interactions involving metasomatic fluids with increasing contributions from inferred recycled oceanic components, leading to the enrichment of V, U, and Fe^{3+}.

At shallower depths (3.5–2.0 GPa), Cr-pyrope type 1 reflects a re-fertilized lherzolite matrix, while the presence of Cr-Ca-rich (green) garnets suggests localized interactions with melted subducted oceanic crust. Furthermore, the occurrence of pyrope and almandine marks the mantle-crust boundary at ~1.3–1.5 GPa, aligning with geophysical Moho estimates in the region. C—S isotopic data obtained with a tentative, early-stage approach, support the influence of recycled crustal materials throughout the mantle column. Ultimately, these findings demonstrate that garnet xenocryst geochemistry is a robust tool for deconstructing the complex thermochemical history of the subcontinental lithospheric mantle.

1. Introduction

Kimberlites and lamproites are unique igneous rocks of paramount economic importance in exploration, being the main source of natural diamonds (Erlank et al., 1987). Their ascent through the mantle can entrap a large cargo of debris mantle xenoliths and xenocrysts (including diamonds) as well as crustal xenoliths (Mitchell, 1995). These rocks can experience a variety of open system processes, including assimilation of phenocrysts and groundmass crystallized from different kimberlite magmas and from the mantle they crossed, and mixing of volatile components (mostly F, H_2O, and CO_2) (Niyazova et al., 2021). The high resistance of garnet xenocrysts to magmatic resorption and weathering favors their preservation in kimberlites, whereas fresh clinopyroxene occurs rarely, especially if rocks are highly altered. Major and minor element composition of garnets (and clinopyroxene) is indicative of pressure and temperature conditions and the type of disrupted peridotite (lherzolite, harzburgite, wehrlite, etc.) (e.g., Griffin et al., 1999; Grütter et al., 2004; Nosova et al., 2025; Waters et al., 1989), while the trace element concentration and fractionation can provide valuable constraints on evolution processes of the lower lithosphere (partial melting, metasomatism, re-fertilization, exsolution) (Coltorti et al., 1999; Griffin et al., 1999, 2009). Therefore, garnet and clinopyroxene xenocrysts from the same kimberlite pipe represent an invaluable source of information on the structure and dynamics of vertical sections of the sub-continental lithospheric mantle (SCLM) down to depths exceeding hundreds of kilometers (Griffin et al., 2009; Le Roex and Class, 2016; Nimis et al.,

* Corresponding author.
E-mail address: bdc@unife.it (C. Bonadiman).

https://doi.org/10.1016/j.lithos.2026.108742
Received 17 April 2026; Received in revised form 15 August 2026; Accepted 17 August 2026
Available online 21 August 2026
0024-4937/© 2026 The Authors. Published by Elsevier B.V. This is an open access article under the CC BY-NC-ND license (http://creativecommons.org/licenses/by-nc-nd/4.0/).

2009).

The Archean cratons constitute the Earth's oldest lithosphere domain (de Wit et al., 1992; Kröner and Hoffmann, 2019). Numerous studies on mantle xenoliths and xenocrysts have been conducted on the Kaapvaal Craton, which extends across South Africa, southern Mozambique, Zimbabwe, Botswana, Namibia, Eswatini, and Lesotho, and where more than 1000 diamond deposits, primary and alluvial, originated from the kimberlite pipes spread on and at the margins of the Kaapvaal Craton (de Wit, 2010). The craton lithosphere is constrained between 180 and 300 km (Eaton et al., 2009, and references therein). However, multiple events, often overlapping, were recorded, leading to thinning and erosion of the mantle roots (Celli et al., 2020; Walsh et al., 2023).

In this study, we analyzed samples from one of the pipes of the Newlands kimberlite, located 50–60 km northwest of Kimberley in the Northern Cape, South Africa. Petrography, as well as major and trace element analysis on kimberlite samples, allows a characterization of the main features of the diamondiferous pipe. In particular, we present geochemical data for garnet and clinopyroxene xenocrysts to constrain composition and thermal evolution of the lithospheric mantle beneath this portion of the craton. Moreover, we provide the first measurements of C and S stable isotopes in garnet xenocrysts to explore the nature of metasomatic fluids and the processes causing isotopic fractionation. The new findings contribute to a better understanding of the petrogenetic evolution of the mantle beneath the Newlands kimberlite and have implications for diamond exploration.

2. Geological setting

The Kaapvaal Craton in southern Africa (Fig. 1a), which consolidated between 3.7 and 2.6 Ga (de Wit et al., 1992), is composed of four

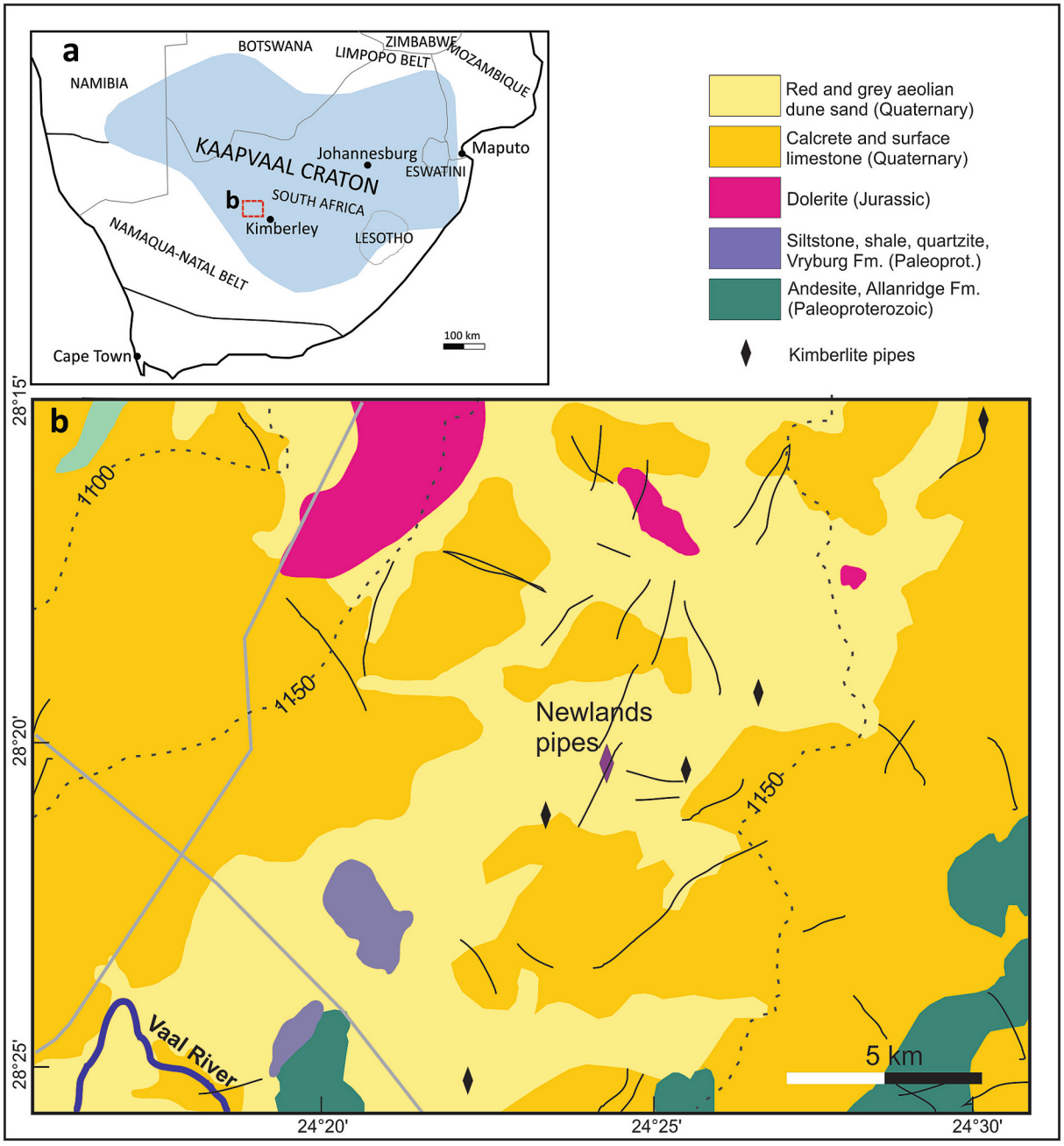


Fig. 1. a) Simplified geological map of southern Africa with extent of the Kaapvaal Craton and the major Proterozoic terranes and belts. b) Detailed geological map of the Newlands area (modified after the '2824 Kimberley' 1:250,000 geological map series, Council for Geoscience).

main domains, as Southern, Central, Pietersburg, and Western terranes (e.g., Donnelly et al., 2012) and is partially covered by basins where thick successions of sedimentary and volcanic rocks were deposited (Kröner and Hoffmann, 2019). The main rocks of the craton range from tonalite gneiss to Archean greenstones and are punctuated by multiple granitic intrusions. More than 200 kimberlite pipes intruded the Kaapvaal Craton between 1800 and 60 Myr, with a major activity during the Mesozoic (Howarth, 2026, and references therein). Kimberlite rocks were historically classified into two types: group I, the most common type worldwide, with high Mg, CO_2, incompatible trace elements, and low Si, Na, and K (Mitchell, 1995; Pearson et al., 2019), and group II, also known as 'orangeites', which are phlogopite-rich rocks with high K/Ti, H_2O, and lower CO_2 (Mitchell, 1995). Other rock names, like Kaapvaal lamproites (Scott-Smith et al., 2018) or olivine lamproites (Pearson et al., 2019) have been proposed for group II. A discussion on the proper terminology goes beyond the scope of this paper, and we refer to the Mitchell (1995) nomenclature for group II. According to Skinner (1989), more than 230 orangeites were mapped in South Africa, Eswatini, and Lesotho, with emplacement ages decreasing from 200 Ma in the north (Dokolwayo) to 110 Ma in the south (Eendekuil).

The Newlands kimberlite is located approximately 50–60 km northwest of Kimberley, in the Northern Cape (coordinates: 28°20'S, 24°02′E, Fig. 1b). It was classified as part of the group II kimberlites (Skinner, 1989), in close vicinity to the similar group II kimberlites of Finsch and Bellsbank. After its discovery in the late 1800's, the diamond production has been intermittent, with an average diamond size of approximately 0.50 carats and an F/G colour grade (Newlands mining staff, personal communication). The mines are located north of the town of Barkly West and follow five 'blows' (pipes) along a 600 m NE-SW-trending system of fissures. These structures become preferential pathways for magma and kimberlite uprising, and a link between kimberlites and rift edges, existing dyke swarms, and fault intersections in structural paths has been proposed (e.g., Menzies et al., 1998).

Although at surface the area is characterized by Quaternary cover, the pipes at Newlands intrude Archean gneiss and Ventersdorp volcanics, and are mostly surrounded by rocks of the Karoo Supergroup (Ecca and Dwyka groups). Host rocks include carbonaceous shales, sandstones, siltstones, and dolerite intrusions. Flood basalts belonging to the overlying Stormberg Group are found as xenoliths within the kimberlites (Le Roex et al., 2003).

A few studies exist on the geochemistry of the Newlands kimberlites: Waters et al. (1989) studied a xenolith at Newlands where a MARID (mica-amphibole-rutile-ilmenite-diopside) portion is in contact with a metasomatized peridotite. Daniels et al. (1995) measured Sr and Nd isotopes on garnets from Newlands, Bultfontein, and Finsch; Menzies et al. (1998) presented a Re—Os study on peridotite xenoliths and garnet macrocrysts; Clarke and Carswell (1977) and Sablukova et al. (2012) analyzed the green macrocrystic garnets that are found only at Newlands and in few other kimberlites in the world, while Ivanic et al. (2012) proposed garnet recrystallization due to decompression. A kimberlite Rb—Sr age at 114 ± 1.6 Ma was measured by Smith et al. (1985), and, more recently, Stanley and Flowers (2016) obtained a zircon/He age with a mean value at 144 ± 12 Ma. In terms of whole rock, Becker and Le Roex (2006) compared the geochemistry of Newlands and other on-craton kimberlites with neighboring off-craton pipes, showing substantial homogeneity among Group II kimberlites, whereas in Group I, a more fertile mantle source is inferred for off-craton compared to on-craton kimberlites.

The rocks of this study were collected at a depth of −120 m in the main pipe (blow 2). The kimberlitic samples are quite homogeneous and do not contain mantle xenoliths, although low-Ca harzburgite and eclogite xenoliths have been documented elsewhere at Newlands (e.g., Dawson and Smith, 1977; Gurney et al., 1991).

3. Analytical methods

Major and trace elements on kimberlite whole rock samples were analyzed by X-ray fluorescence (XRF) and inductively coupled plasma-mass spectrometry (ICP-MS). Mineral separation provided approximately 200 garnets and clinopyroxenes. On these minerals, major elements were collected in situ via electron probe microanalyzer (EPMA), and trace elements through laser ablation-inductively coupled plasma-mass spectrometry (LA-ICP-MS). Carbon and sulfur elemental and isotopic analyses were performed on single grains of garnet through elemental analyzer-continuous flow-isotopic ratio mass spectrometry (EA-CF-IRMS). Details on analytical procedures and obtained results are in supplementary data (Analytical Techniques and Tables S1 – S6).

4. Results

4.1. Whole rock

The three analyzed kimberlitic samples are porphyritic and exhibit equigranular texture with rounded to euhedral olivine crystals. Three polished thin sections were observed under the microscope, and olivine reaches sizes of several millimeters across. Nearly all olivine crystals show signs of serpentinization along the rims and fractures. Additionally, macrocrysts of phlogopite, chromite, and magnetite as well as host rock clasts, can be identified within a fine-grained groundmass of calcite, phlogopite, and serpentine, among other minerals. No garnet could be identified in the thin sections for this study. However, mineral separation provided a relatively high content of garnet crystals.

The major element oxides of the three collected samples are reported and plotted in Fig. 2 as determined without normalization to a volatile-free basis. Samples are ultrabasic with 36.3 to 39.8 wt% SiO_2 and MgO ranging from 26.2 to 29.5 wt%. Further variations in major element compositions are as follows: CaO (6.00–8.06 wt%), Al_2O_3 (1.71–3.43 wt %), Fe_2O_{3t} (6.45–7.98 wt%), Na_2O (0.06–0.24 wt%), K_2O (1.63–2.86 wt %), TiO_2 (0.45–0.60 wt%), P_2O_5 (0.65–1.14 wt%), and MnO (0.14–0.20 wt%).

The Newlands samples can be classified as typical group II kimberlites, such as Finsch and Bellsbank (Fig. 2). Major and trace elements are shown in Table S1. The relatively higher K_2O contents compared to other literature data are attributed to the heterogeneity of the rock samples, characterized by variable proportions of host rock silicate clasts, mainly feldspathic in composition. Different amounts of feldspar are in fact observed in thin sections, but the trace element patterns are comparable in the 3 samples. The primitive mantle-normalized trace element diagram (Fig. S1a) shows negative anomalies of Ba, K, P, Zr, and

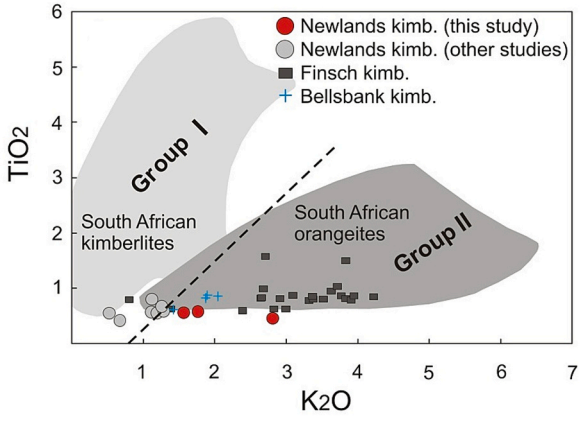


Fig. 2. TiO_2 vs K_2O. Kimberlite type boundaries and fields of South African kimberlites and orangeites (after Smith et al., 1985). Additional Newlands, Finsch and Bellsbank kimberlite data from Smith et al. (1985), Fraser and Hawkesworth (1992), Becker and Le Roex (2006).

Ti and positive anomalies of Pb and Nd. The chondrite-normalized rare earth element (REE) diagram (Fig. S1b) shows the Newlands samples in comparison to other South African kimberlites. All three samples are strongly light (L) REE enriched [$(La/Sm)_N$ = 11.8–13.1; $(La/Yb)_N$ = 123–326], and exhibit almost flat heavy (H)REE patterns, and slightly negative Eu anomalies ($Eu/Eu^* = Eu_N/\sqrt{(Gd_N + Sm_N)}$ between 0.80 and 0.84).

4.2. Xenocryst population

4.2.1. Cr-diopside

Due to the high degree of alteration, fresh clinopyroxene rarely occurs in kimberlites, although fresh grains tend to be more abundant at greater depths. The majority of clinopyroxene ranges from 0.5 mm to 2 mm in length and shows typical bright emerald-green colour (Fig. 3). It exhibits high Ca# [Ca/(Ca + Mg) atomic ratio, 0.45–0.49], high Mg# [$Mg/(Mg + Fe^{2+})$ atomic ratio, 0.93–0.95], and appreciable sodium content (1.57–3.81 wt% Na_2O), correlated with relatively high chromium (1.78–3.85 wt% Cr_2O_3) and aluminum (0.87–3.58 wt% Al_2O_3), along with increasing intensity of greenish tint. TiO_2 varies from 0.02 to 0.23 wt% (Tables 1 and S2). Despite the restricted range of total iron contents (FeO_t = 1.15–2.64 wt%) Fe_2O_3, calculated by stoichiometry (Neave et al., 2024) is highly variable (Fe_2O_3 = 0–1.13 wt%; Table S2).

Clinopyroxene nomenclature was verified through QJ vs. Ca–Mg–Fe CPX (Fig. S2a; Morimoto, 1988). The samples plot in the diopside field (71–88%), with discrete contributions of jadeite (6–17%) and kosmochlor (6–12%) (Fig. S2b and Table S2). Clinopyroxene with this composition is generally referred to as Cr-diopside. The Na-Cr-Al ternary plot is in Fig. S3.

Chondrite-normalized REE patterns of clinopyroxene (Fig. 4a) show systematically decreasing abundances between Nd and Lu. The patterns of all grains show a notable hump in Nd_N and slightly positive to negative LREE patterns [$(La/Nd)_N$ = 0.52–2.3]. The patterns of px-40 and px-161 show the highest enrichment in LREE and the most prominent steep slope in the M-HREE, which reflect the remarkably low concentrations of these elements. Primordial mantle-normalized minor and trace elements selected in decreasing order of chalcophile behavior (Fig. 4b) show a general Th enrichment (Th_N = 1.3–13.1), correlated with a relative Pb enrichment (Pb_N = 1.0–19.1), while Sc and V show the same range of enrichment (2–6 times PM values).

4.2.2. Garnet

The Newlands garnets were classified based on the calculated end-member scheme of Locock (2008) and the accepted IMA nomenclature for the garnet supergroup (Grew et al., 2013). 184 out of 189 analyzed grains are represented by the pyrope-almandine series with a wide range of mole fractions of the main garnet species (Tables 1 and S2).

This series (140 out of 189) is classified as pyrope ($Prp_{0.41–0.76}$; $Alm_{0.08–0.38}$; $Grs_{<0.17}$; $And_{<0.04}$; Prp: pyrope, Alm: almandine, Grs: grossular, And: andradite) with the majority (104 out of 140) with $Cr_2O_3 \geq 1$ wt%, therefore attributable to the Cr-pyrope subgroup Griffin et al., 1999). A significant number of grains (44 out of 189) are classified as almandine with a significant amount of pyrope components ($Prp_{0.35–0.38}$; $Alm_{0.43–0.45}$; $Grs_{<0.16}$; $And_{<0.02}$). Five green, relatively large (up to 3 mm-long) crystals fall in the uvarovite ((Uv) field (Fig. 5, Table S2), having the highest Ca^{2+}/R^{2+} and the highest Cr^{3+}/R^{3+} admitted for Ca-Mg/Cr-Al solid solution ($Prp_{0.34–0.40}$; $Uv_{0.33–0.34}$; $Alm_{0.07–0.09}$; $Grs_{0.11–0.19}$; $And_{<0.05}$). This composition will be referred as Cr-Ca-rich garnet.

Compared to Primordial Mantle (PM), all garnets are strongly depleted in large ion lithophile elements (LILEs, e.g., Rb, Ba, and Sr) but variably enriched in V and Sc and high-field strength elements (HFSEs, e.g., Nb, Ta, Zr, Hf, and U—Th) (Table S3). As a whole, the garnet grains contain low to very low total REE (ΣREE max 60 ppm in Cr-Ca-rich garnets).

4.2.2.1. Cr-Ca-rich garnet. Cr-Ca-rich garnet occasionally occurs as grain in diamondiferous kimberlite bodies or, rarely, associated with peridotite xenoliths (Sablukova et al., 2012). It plots in the Ca-rich field of the Ca-Mg-Fe^{2+} classification diagram, with Cr occupying the Y site (Fig. 5; Grew et al., 2013). These grains were reported for the first time in a Newlands pipe by Clarke and Carswell (1977).

Backscattered images collected at the SEM show that this garnet type is generally unzoned, although darker rims and patched zoned can be locally visible (Fig. S4). The high-Cr, high-Ca garnet population shows a narrow range of Mg# (Mg# = molar $Mg/(Mg + Fe^{2+})$) between 0.80 and 0.83, corresponding to mantle-derived garnets (Fig. 6a). The TiO_2 content (0.27–0.33 wt%) is consistently low, as expected for unmetasomatized mantle-derived Cr-pyrope (Fig. 6b). Notably, this group is characterized by the highest Fe^{3+} (Fe_2O_3 = 1.06–1.73) as stoichiometrically determined (Table S2; Locock, 2008) and by anomalously high redox–sensitive trace elements such as U (up to 1.2 ppm) and V (up to 470 ppm). Four out of five grains have overlapping chondrite-

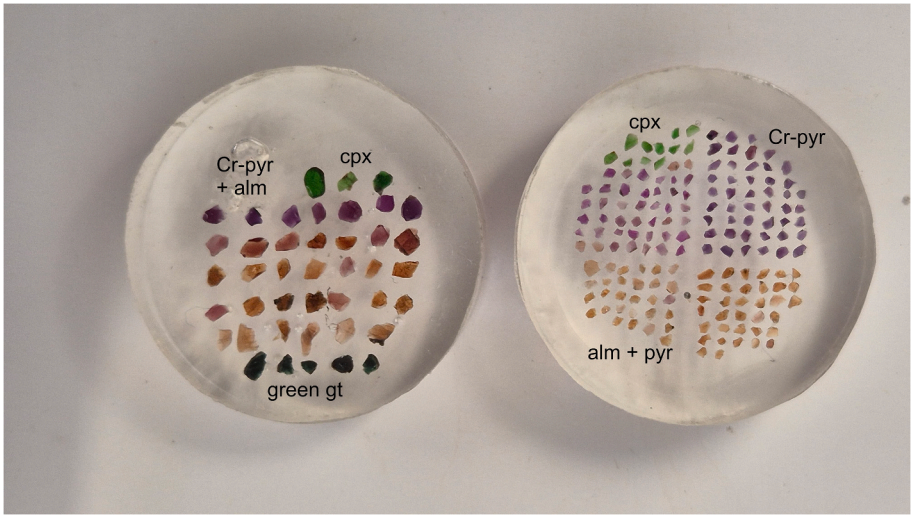


Fig. 3. One-inch diameter (2.54 cm) mounts with clinopyroxene and garnet analyzed for major and trace elements. Cr-diopside is the green grains on top. Green garnet (n = 5) is bottom left. All other grains are almandine, pyrope, and Cr-pyrope garnet. (For interpretation of the references to colour in this figure legend, the reader is referred to the web version of this article.)

Table 1
Average composition (EMPA and LA-ICP-MS) of Cr-diopside and garnet types. n = numbers of analyses; values in italics refer to single LA-ICP-MS detectable concentration.

	Cr-diopside			Uvarovite-rich		Almandine		Pyrope		Cr-pyrope type1		Cr-pyrope type2		Cr-pyrope type3		Cr-pyrope type4	
(wt%)	average (n = 14)	Std Dev	(wt%)	average (n = 5)	Std Dev	average (n = 44)	Std Dev	average (n = 36)	Std Dev	average (n = 49)	Std Dev	average (n = 23)	Std Dev	average (n = 22)	Std Dev	average (n = 10)	Std Dev
SiO2	55.57	0.16	SiO2	39.56	0.21	40.02	0.36	42.10	0.86	42.34	0.46	42.27	0.60	42.36	0.59	43.43	0.11
TiO2	0.15	0.07	TiO2	0.29	0.02	0.29	0.08	0.38	0.12	0.27	0.13	0.09	0.06	0.03	0.02	0.01	0.01
Al2O3	2.45	0.67	Al2O3	13.80	0.17	21.94	0.12	22.52	0.46	19.50	2.27	18.24	1.88	18.33	1.13	19.76	0.13
Cr2O3	3.10	0.70	Cr2O3	11.22	0.15	0.04	0.01	0.39	0.26	5.42	3.13	7.50	2.36	7.54	1.23	6.39	0.10
FeOt	2.06	0.34	FeO	5.06	0.31	22.51	2.47	12.81	3.70	7.63	1.85	6.80	0.53	6.63	0.50	5.59	0.04
MnO	0.08	0.02	MnO	0.32	0.02	0.46	0.06	0.35	0.07	0.36	0.05	0.36	0.05	0.36	0.06	0.27	0.01
MgO	15.45	0.89	MgO	9.41	0.72	9.72	0.74	17.60	3.18	20.39	1.05	20.63	1.36	21.00	2.03	25.18	0.12
CaO	18.95	1.35	CaO	20.67	1.10	6.16	1.26	4.96	1.38	5.15	0.73	5.24	1.35	4.88	2.20	0.60	0.02
Na2O	2.75	0.63	Na2O	0.03	0.01	0.11	0.03	0.08	0.02	0.05	0.02	0.02	0.01	0.01	0.01	0.01	0.01
NiO	0.04	0.01	NiO	0.01	0.01	0.02	0.01	0.02	0.01	0.02	0.01	0.02	0.01	0.01	0.00	0.01	0.01
Total	100.59		Total	100.37		101.29		101.22		101.13		101.17		101.16		101.25	
(ppm)			(ppm)														
Sc	51.6	21.4	Sc	322.	58.7	52.1	21.4	59.3	13.2	110	25.0	121	30.2	118.	16.0	95.4	0.901
V	380	107.	V	435.	23.9	92.9	17.28	150	32.8	242.	74.5	262	92.1	275.	59.4	166.	3.68
Cr	21,033	4920.	Cr	73,974.128	1554	272.	83.5	2392	1540.	34,122.	20,140	47,306	15,126	47,515	7990.	40,060	661
Ni	312.	33.4	Ni	40.2	1.92	28.4	8.15	44.7	8.76	43.2	9.05	41.5	7.60	40.6	7.34	42.5	0.302
Rb	0.49	0.60	Rb	3.06		0.511	0.595	2.85	6.10	0.068	0.014	0.637		bdl		0.440	0.523
Sr	363	131	Sr	8.24	13.1	1.29	1.48	1.74	5.04	0.608	0.620	1.174	0.896	1.94	2.20	3.29	2.95
Y	1.93	1.52	Y	21.4	7.93	113	331	20.3	13.2	10.7	4.11	3.00	1.21	0.793	0.304	0.148	0.027
Zr	41.4	36.1	Zr	42.7	17.2	13.1	0.949	27.6	14.	30.7	21.3	16.4	13.0	9.06	8.988	0.247	0.242
Nb	0.73	0.40	Nb	5.036	0.932	0.129	0.202	0.214	0.428	0.279	0.205	0.432	0.180	0.443	0.205	0.229	0.194
Sb	bdl		Sb	*0.047*		*0.055*		0.0805	0.011	*0.047*		*0.138*		bdl		bdl	
Ba	1.40	1.37	Ba	13.9	24.0	5.47	8.79	29.2	84.1	0.179	0.325	4.20	7.22	0.077	0.118	2.17	4.16
La	11.4	7.82	La	1.09	0.874	0.0801	0.173	0.131	0.3569	0.067	0.077	0.141	0.115	0.216	0.134	0.429	0.661
Ce	33.3	19.3	Ce	7.67	0.402	0.326	0.331	0.346	0.670	0.623	0.639	1.462	0.985	2.19	1.33	1.38	1.21
Pr	4.73	2.25	Pr	2.231	0.503	0.092	0.076	0.081	0.078	0.217	0.176	0.477	0.275	0.618	0.292	0.181	0.109
Nd	20.1	8.02	Nd	16.09	5.65	0.875	1.087	0.695	0.374	1.84	1.36	3.84	2.04	4.31	2.73	0.666	0.298
Sm	3.52	1.78	Sm	3.99	1.69	1.43	1.589	0.700	0.290	1.18	0.74	1.29	0.817	0.907	0.579	0.167	0.031
Eu	0.90	0.50	Eu	1.025	0.425	0.630	0.125	0.386	0.159	0.471	0.291	0.411	0.3075	0.212	0.136	0.021	0.0067
Gd	2.16	1.20	Gd	2.641	0.99	6.70	14.9	1.67	0.662	1.67	0.961	1.01	0.716	0.445	0.309	0.051	0.025
Tb	0.18	0.12	Tb	0.359	0.120	1.98	5.34	0.364	0.162	0.286	0.146	0.102	0.054	0.040	0.030	0.006	
Dy	0.66	0.48	Dy	2.84	0.975	17.4	49.3	3.09	1.68	1.96	0.853	0.555	0.231	0.157	0.095	0.020	0.007
Ho	0.08	0.06	Ho	0.764	0.278	3.85	11.0	0.751	0.477	0.403	0.155	0.108	0.042	0.029	0.011	0.006	0.002
Er	0.16	0.13	Er	3.28	1.25	11.7	33.0	2.60	1.83-	1.24	0.484	0.372	0.158	0.113	0.046	0.032	0.004
Tm	0.03	0.02	Tm	0.621	0.254	1.64	4.57	0.401	0.301	0.181	0.075	0.062	0.030	0.029	0.012	bdl	
Yb	0.08	0.08	Yb	5.91	2.45	10.9	30.0	2.95	2.25	1.33	0.531	0.5234	0.277	0.277	0.128	0.124	0.0167
Lu	0.01	0.01	Lu	1.17	0.478	1.48	3.94	0.459	0.362	0.209	0.081	0.100	0.050	0.062	0.027	0.033	0.002
Hf	1.57	0.91	Hf	0.853	0.289	0.223	0.053	0.475	0.255	0.641	0.423	0.322	0.223	0.191	0.183	0.0075	0.006
Ta	0.07	0.04	Ta	0.478	0.183	0.013	0.014	0.018	0.028	0.024	0.019	0.029	0.018	0.027	0.015	0.005	0.0056
Pb	1.00	0.76	Pb	0.275	0.268	0.077	0.051	0.352	0.432	0.039	0.0015	bdl		*0.044*		*0.228*	
Th	0.32	0.29	Th	0.747	0.070	0.014	0.036	0.028	0.058	0.023	0.024	0.043	0.028	0.0823	0.0654	0.036	0.077
U	0.05	0.05	U	0.979	0.428	0.009	0.012	0.010	0.012	0.039	0.039	0.079	0.063	0.125	0.104	0.013	0.017

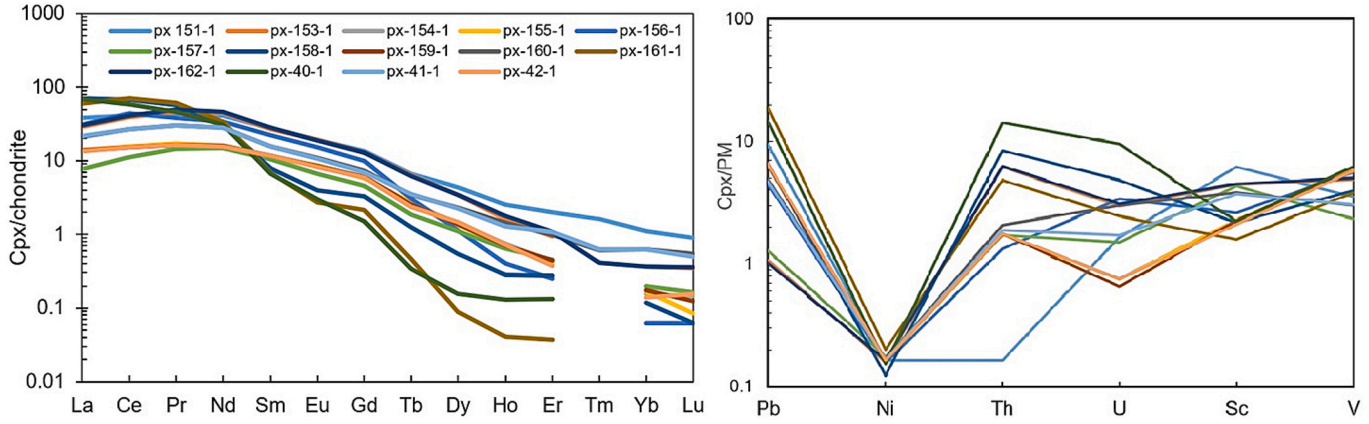


Fig. 4. a) CI Chondrite normalized Rare Earth Elements (REE) and selected trace metal. b) Primitive Mantle (PM) normalized patterns of Newlands Cr-diopside xenocrysts. Non-plotted values are below detection limit. CI Chondrite and PM values from McDonough and Sun (1995).

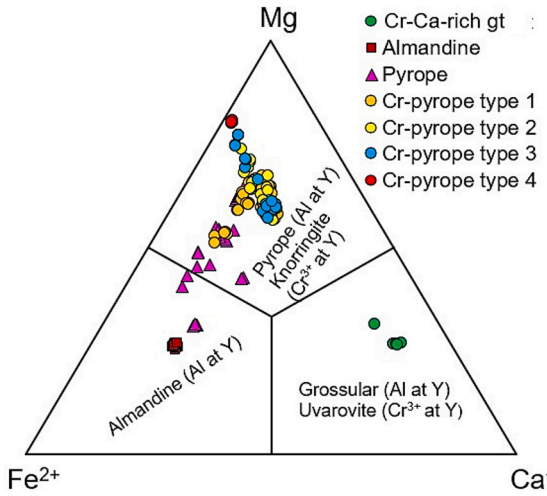


Fig. 5. Ternary diagram, based on X (Ca, Fe^{2+} and Mg) occupancy, showing end-member composition of Newlands garnet (after Grew et al., 2013). The sum of all end-members range from 93 to 99%. End-members calculated according to Locock (2008).

normalized humped L-Middle(*M*)REE (MREE = Sm to Dy) profiles, with a peak in Nd_N and a through in Tb_N, with avg. $(La/Nd)_N = 0.073$, $(Sm/Dy)_N = 2.39$, and positive slope from MREE to HREE [(avg $(Dy/Yb)_N$ = 0.24]. Grain gt-2.1 displays a distinct REE profile with almost flat LREE ($La_N = 7.24$, $Nd_N = 8.44$), slightly positive M-HREE patterns [$(Dy/Yb)_N$ = 0.36], and U and Th comparable to the rest of the garnet population (Fig. 7a; Tables 1, S2 and S3).

4.2.2.2. Almandine-pyrope. Almandine is orange to light purple, with constant Mg# (0.44–0.46) and TiO_2 (0.28–0.35 wt%), with Cr at ppm level (263–382 ppm Tables 1, S2 and S3). Almandine shows low ΣREE (16–21 ppm), relatively flat M-HREE patterns [$(Dy/Yb)_N = 0.78–1.31$], and variably positive to negative slopes for LREE patterns (La_N = 0.05–2.27; $Ce_N = 0.17–1.90$, Fig. 7b and Table S3). At increasing Mg/Fe ratios, a group of orange garnets plots at the almandine-pyrope boundary or into the proper pyrope field (Fig. 5). Ten grains in the pyrope field with Mg# in the range 0.67–0.74 show Ca# (Ca/(Ca + Mg) molar) negatively correlated with Mg# (Fig. 6a), and the lowest Ti of this group (TiO_2 = 0.21–0.27 wt%) (Fig. 6b). Pyrope with the lowest Ca# and the highest Mg# also has the highest Ti and Cr contents (TiO_2 = 0.58 wt%, Cr_2O_3 = 0.67–0.96 wt%), approaching the composition of the Cr-pyrope group (Fig. 6a, b and Table S2). Despite the large range of Mg# values, this group shows similar M-HREE profiles, with patterns from flat to positively sloped [$(Dy/Yb)_N$ = 0.63–0.98], with variably LREE enrichments (La_N and Ce_N in the range 0.01–4.54 and 0.06–3.02, respectively, Fig. 7c). Rare Earth Element profiles of the pyrope group mirror the grains of the almandine group, but pyrope shows a larger element range than almandine. A few grains of this garnet series show anomalously high La-Ce(—Pr). Because garnet strongly discriminates against incompatible LREEs, these elements are modified by late-stage

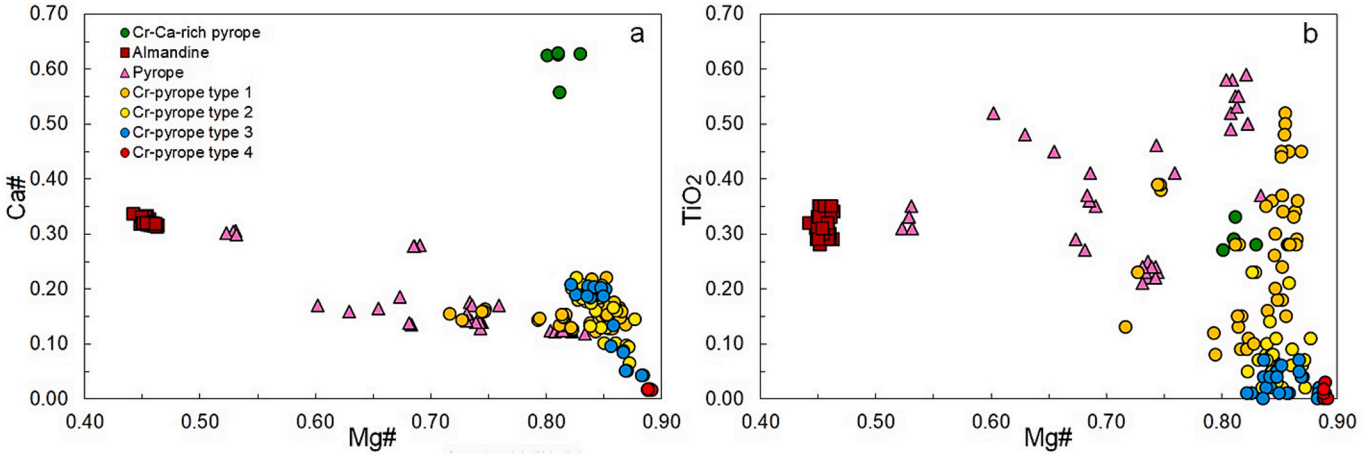


Fig. 6. a) Mg# vs Ca# and b) Mg# vs TiO_2 for garnet.

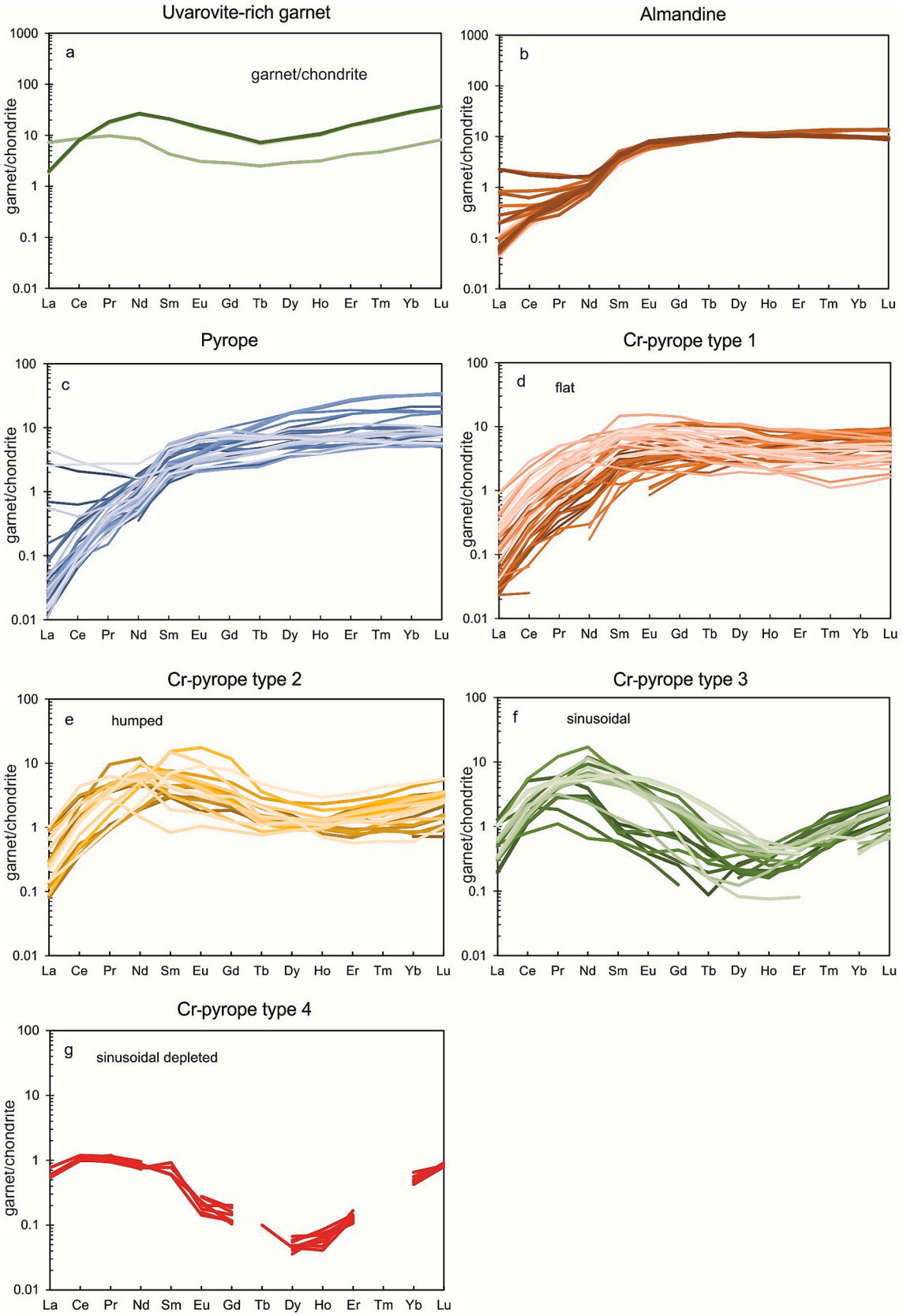


Fig. 7. a-g. Cl chondrite-normalized REE patterns of the various garnet groups from Newlands kimberlite. The largest group of Cr-pyrope shows four district REE profiles (d-g). Non-plotted values are below detection limit. CI chondrite values from McDonough and Sun (1995).

'host rock' interactions (e.g., Griffin et al., 2002).

4.2.2.3. Cr-pyrope. Purple grains represent the largest group among the Newlands garnets (Table 1). This group plots into the pyrope field in Fig. 5 and was classified according to MgO and Cr_2O_3 contents (>1 wt%) as Cr-pyrope. Mg# values span in the range 0.72–0.89 with Cr contents between 1.35 and 10.9 wt%. Ca# is negatively correlated with Mg#, testifying for the lithological control of garnets (Fig. 6a). Instead, Ti is not primarily correlated with Mg#, but systematically decreases from type 1 to type 4 (avg TiO_2 type 1 = 0.27; type 2 = 0.09; type 3 = 0.03; type 4 = 0.01) (Fig. 6b). Overall, Cr-pyrope is characterized by relatively low REE contents (ΣREE = 2.12–24.4 ppm). Four Cr-pyrope types were distinguished (Fig. 7 d-g):

Cr-pyrope type 1: Irrespective of the Cr contents, the majority of these grains are M-HREE enriched (3–8 times chondrites) with relatively flat M-HREE patterns [avg $(Dy/Yb)_N$ = 1.01] and strongly depleted LREEs [avg $(La/Nd)_N$ = 0.06, Fig. 7d and Table S3].

Cr-pyrope type 2: The REE show a humped trend, with positive slopes from LREE to MREE [avg $(La/Nd)_N$ = 0.09, Fig. 7e] with peaks in Sm and Eu, followed by negative slopes from MREE to HREE, a trough in Dy and Ho, and a weak positive slope from Dy to Yb and Lu [avg $(Dy/Yb)_N$ = 0.90]. Yttrium is generally <5 ppm (max 7.22 ppm).

Cr-pyrope type 3: The REE pattern is sinusoidal (Fig. 7f), with enrichment from LREE to MREE [avg $(La/Nd)_N$ = 0.18], a marked trough in Dy and Ho, and a positive slope for HREE [avg $(Dy/Yb)_N$ = 0.51]. These grains also show low to very low Y (ranging from 0.09 to 1.28 ppm).

Cr-pyrope type 4: Ten grains, with the highest Mg# values (0.89) and the lowest CaO contents (max. 0.63 wt%), show sinusoidal REE patterns with vg $(La/Nd)_N$ = 0.97, $(Sm/Dy)_N$ = 15.8, $(Dy/Yb)_N$ = 0.11. This group also shows the lowest REE (ΣREE = 2.12–9.69 ppm), with the highest normalized values reaching ~1× chondrite only for Ce, Pr, and Nd (Fig. 7g).

4.3. Garnet C and S isotopes

Carbon and sulfur in garnets are present at trace/ultratrace levels; for this reason, isotopic analyses required quite large amounts of material, and, given the scarcity of Cr-Ca-rich garnet, C and S isotopic measurements were possible only for almandine, pyrope, and Cr-pyrope (Table S4). In order to maximize the collection of data, the grains were not reduced to powder (Analytical Techniques in supplementary material).

The highest C content was recorded in almandine (0.11 wt%), whereas pyrope and Cr-pyrope display values from 0.07 to 0.10 wt%. The associated carbon isotopic ratios ($\delta^{13}C$) of pyrope, Cr-pyrope, and almandine fall within a narrow range, from −24‰ to −16‰ (Table S4).

A global compilation of kimberlite carbonate data, including Kimberley, shows $\delta^{13}C$ in the range − 11.9 to +0.2‰ (Giuliani et al., 2014).

Sulfur content in measured garnets is close to the instrument detection limits. In order to obtain reliable isotopic ratios, we made up for the low contents by processing a large amount of sample material. The S isotopic compositions for pyrope, Cr-pyrope, and almandine record similar $\delta^{34}S$ values (ca. -3.2‰), which is in agreement with the values obtained from in-situ sulfide and bulk-rock samples from the Bultfontein kimberlite ($\delta^{34}S$: −5.9 to −1.4‰; Giuliani et al., 2016) and close to the upper limit (range $\delta^{34}S$: −5.7 to −3.4‰) obtained from magmatic Ni-Fe-Cu sulfides in low-S fresh kimberlite from Kimberley (Fitzpayne et al., 2021).

5. Discussion

5.1. Geothermobarometry and P-T paths

On the basis of the Na-Cr-Al ternary plot, clinopyroxene represents a phase equilibrated in the source region of kimberlite-forming melt (Fig. S3; Stachel et al., 2022). The P-T conditions for Cr-diopside were obtained from the iterative calculations in the PTEXL spreadsheet (https://cms.eas.ualberta.ca/team-diamond/downloads/), using the Cr-in-cpx barometer of Sudholz et al. (2021a) in combination with the cpx thermometer of Nimis and Taylor (2000) (Table S5). The equilibrium conditions for clinopyroxene correspond to T = 774–1012 °C, at pressures between 3.6 and 4.9 GPa. Errors on P and T estimates are assumed to be ±0.2 GPa and ± 30 °C, respectively.

More complex is the P-T estimation when dealing with garnet. In a peridotitic mantle, the temperature dependence of Ni partitioning between garnet and olivine is well known since the pioneering studies of Griffin et al. (1989) and Ryan et al. (1996). The Ni content of mantle olivine usually varies over a restricted range (2800–3200 ppm, Ryan et al., 1996) in comparison with a higher variability of Ni in mantle garnet (10–200 ppm, Nimis et al., 2024). Various formulations have been proposed over time and they are continuously amended (Nimis et al., 2024, and references therein). In this paper, we constrain the temperatures for Cr-pyrope through the Ni-in-garnet thermometer (e.g., Canil, 1999; Ryan et al., 1996). Although the consistency between the different versions of this and other well-tested thermometers for peridotites is still debated (Nimis et al., 2024, and references therein), this thermometer has the advantage of being relatively insensitive to P. We evaluated the more recent calibrations proposed by Sudholz et al. (2021b) and Nimis et al. (2024). The Sudholz et al. (2021b) geothermometer provides some improvement at high temperature relative to Canil (1999), but with lower precision. In addition, it is not calibrated for the composition of green garnets, particularly Ca–Cr-rich garnets, which are present in our dataset. The equation proposed by Nimis et al. (2024) includes pressure as an input parameter and therefore requires iterative calculations. We therefore follow the suggestion of Nimis et al. (2020), according to which averaging T-Ryan et al. (1996) and T-Canil (1999) produces T estimates that are more consistent with those obtained for clinopyroxene. Errors on T estimates are assumed to be ±50 °C, considering uncertainties of the geothermometer and propagation of analytical and P errors (±0.4 GPa; Nimis et al., 2024).

The pressure estimates from garnet were determined using the empirical calibration of the Cr/Ca-in-garnet barometer of Grütter et al. (2006). This calibration is valid for Cr-pyrope with Cr_2O_3 > 1 wt% and Mg# in the range 75–96 and in equilibrium with spinel. As a result, this approach can only determine the minimum pressure of garnet xenocrysts (unknown mineral assemblage).

The choice of the most appropriate geothermometer and geobarometer in garnet was also facilitated by the indications obtained from the nomenclature diagram of Grütter et al. (2004) (Fig. 8).

Almandine and pyrope groups cluster between the G4 low-Cr pyroxenitic and the G3 eclogitic fields. Overall, the Ni contents vary from 17 to 66 ppm (almandine and pyrope), but the majority have Ni in the narrow range of 34–60 ppm (Fig. S5). The Ni-in-garnet geothermometer and Cr-in-garnet geobarometer cannot be applied to these garnets, since the coexistence with mantle olivine is highly debatable and most grains are Cr-free with Mg# <0.75, i.e., well above the garnet-spinel mantle transition (Tables 1, S2 and S3). LA-ICP-MS analyses confirm the presence of zircon inclusions in a few almandine/pyrope grains, therefore we assume that ideally the entrapment P-T conditions may be consistent with phase equilibria (Zhong et al., 2019). At the first stage of reasoning, we applied the $P_{inclusion}$ formulation proposed by Zhong et al. (2019) and the Ti in garnet geothermometer (Kawasaki and Motoyoshi, 2016), assuming that the relatively high percentages of pyrope component in the almandine group suggest the potential equilibrium with orthopyroxene, as in the Kawasaki and Motoyoshi (2016) calibration. We applied the proposed formulations to the Newlands almandine/pyrope group and, with high caution we inferred the P-T range of equilibrium conditions. Combining the reported P-T uncertainties of the original formulations, we propose cumulative P-T errors of ±0.5 GPa and ± 50 °C, respectively. The resulting P-T conditions are constrained at 823–849 °C

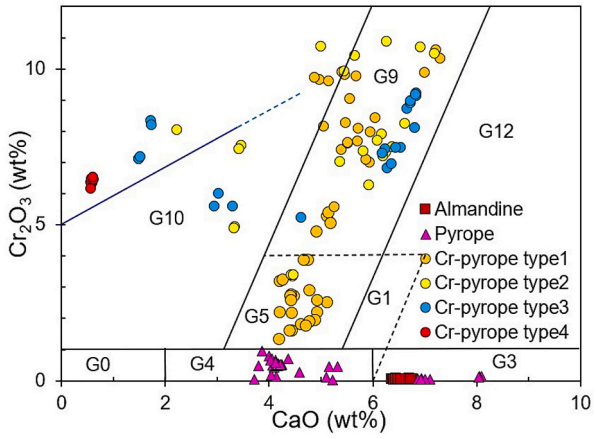


Fig. 8. G-number nomenclature of the Cr_2O_3 vs. CaO diagram (after Grütter et al., 2004). G3 and G4 eclogite and low-Cr pyroxenite fields; G5 (Mg number < 0.73) and G9 (Mg number > 0.73) lherzolite; G10 harzburgite; G12 wehrlite; G1 megacryst; G0 unknown. The blue line in G10 corresponds to the graphite/diamond boundary of Grütter and Sweeney (2000). (For interpretation of the references to colour in this figure legend, the reader is referred to the web version of this article.)

and 1.33–1.35 GPa for almandine and 882–1023 °C and 1.39–1.52 GPa for pyrope (Fig. 9a and Table S5) and correspond to the crust-mantle boundary (35–40 km depth) as obtained by Ps Moho conversions beneath a grid over an area of about 65 × 50 km, which includes sites near Newlands (James, 2007), and is also in agreement with the large amount of crustal xenoliths observed in the field during sampling.

The largest group of Cr-pyropes has Ni in the small range of 24–56 ppm, overall overlapping the contents of the pyrope group, with no correlation with the Cr contents (Fig. S5). These features reflect an overall limited temperature fluctuation (T = 863–1079 °C; average: 1000 ± 47 °C; Table S5) compared to P (1.87–4.33 GPa). However, most of the Cr-pyrope type 1 (flat M-HREE and highly depleted LREE) plots into the G5 (pyroxenite) and G9 (lherzolite) cells in Grütter et al. (2004), whereas Cr-pyrope types 2, 3, and 4 (humped and sinusoidal REE profiles) have Cr—Ca contents and Mg# that encompass the pyroxenite (G5), lherzolite (G9), and harzburgite (G10) fields (Fig. 8).

Cr-pyrope type 4 and a few of type 3 record the highest equilibration pressure (4.5–4.9 GPa), crossing the graphite/diamond transition (Day, 2012). This is in agreement with the P-T calculated for Cr-diopside and supports a rather cold geotherm between 37 and 40 mW/m^2 (Hasterok and Chapman, 2011). The resulting depth (adopting a factor of 32 km per 0.1 GPa; Nimis et al., 2020) is constrained between 145 and 155 km (Fig. 9a).

However, most of the Cr-pyrope types 1, 2, and 3 plot well above the 40 mW/m^2 model conductive geotherm with temperatures in the relatively narrow range of 860–1080 °C and pressures between 1.8 and 4.1 GPa (Fig. 9a). We infer that this disequilibrium was induced by metasomatic effects, likely accompanied by a major decompression event leading to garnet recrystallization (e.g., Griffin et al., 2009; Ivanic et al., 2012). Such disruption of the equilibrium conditions, with xenocrysts spanning from the diamond-bearing mantle towards the mantle/crust boundary region, suggests that, for the large majority of the Newlands garnets, the application of a routine procedure to project garnet temperature onto a 'known' geotherm remains rather speculative.

The Ni-in-garnet geothermometer and the empirical Cr/Ca-in-garnet geobarometer are not calibrated for Cr-Ca-rich pyropes, and no P-T algorithms have been proposed so far. We assume that their Ni and Cr contents are nevertheless still sensitive to temperature and pressure, and we tentatively calculated P-T conditions at ~2.6 GPa and ~ 1000 °C, similar to the majority of Cr-pyrope type 1, not equilibrated along any modelled geotherm (Fig. 9a), and in agreement with previous estimates

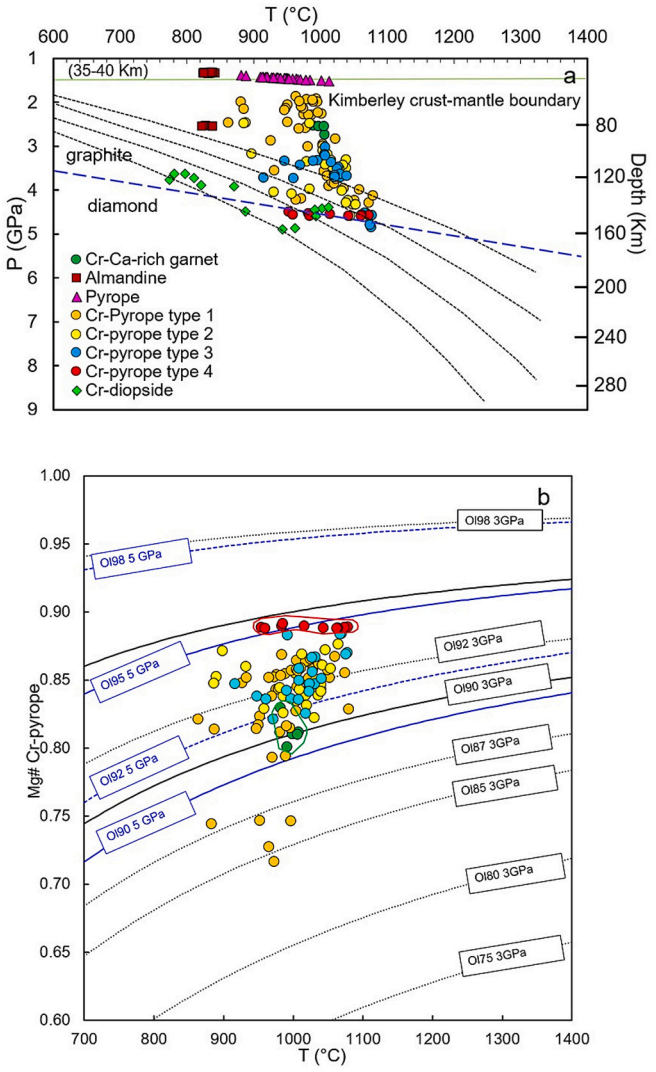


Fig. 9. a) P-T estimates for cpx and gt xenocrysts. P-T parameters for Cr-pyrope and Cr-Ca-rich garnet were calculated through the Ni-in-garnet equilibrium, averaging T-Ryan et al. (1996) and T-Canil (1999) (Canil, 1999; Ryan et al., 1996; Sudholz et al., 2021b) and empirical barometer of Grütter et al. (2006); for almandine and pyrope P-T were calculated using the EoS parameters of the equilibrium pyrope-almandine solid solution (Zhong et al., 2019), whereas for Cr-diopside P-T were obtained by the Cr-in-cpx barometer of Sudholz et al. (2021a) combined with the cpx thermometer of Nimis and Taylor (2000). Calculated geotherms (35 to 45 mW/m^2) are according to Hasterok and Chapman (2011). The blue dashed line marks the transition from graphite to diamond stability field. b) Calculated mantle olivine Mg# in equilibrium with the studied garnets (Griffin et al., 1999). The equilibrium temperatures were obtained using the geothermometers of Canil (1999) and Ryan et al. (1996) as in a). Ideal olivine Mg# equilibrium lines between Mg# = 0.89 and Mg# = 1.00 are calculated at 5 GPa (blue lines) and 3GPa (black lines). Ideal olivine Mg# equilibrium lines below 0.89 are calculated at 3GPa. References for calculations after O'Neill and Wood (1979), and Gaul et al. (2000).
The red contour shows that Cr-pyrope type 4 is equilibrated at 5GPa with olivine with Mg# = 0.95, in agreement with the previously calculated garnet pressure. The arrow indicates the progressive interactions with metasomatic melts. Interesting to note that the Ca-Cr-rich (green) garnet is in equilibrium with olivine with Mg# = 0.92 at ~3GPa, supporting progressive re-fertilization of the Newlands peridotite domain. Five type 1 garnets show remarkable effects of interactions with host melts. (For interpretation of the references to colour in this figure legend, the reader is referred to the web version of this article.)

for Cr-Ca-rich garnets (e.g., Nosova et al., 2025, and references therein).

5.2. Sampling the Kaapvaal mantle roots

The Newlands kimberlite pipes are characterized by their scarcity of discrete xenoliths. The xenoliths described by Ivanic et al. (2012) appear as monogranular garnet samples or polygranular samples with garnet between 60 and 90% in an ol + opx altered matrix. Sablukova et al. (2012) report two 'peridotites' with a composition of gt 50–70%, ol 28–20%, sp. 2–20%, and textures resembling mineral aggregates with melt embayments. On the other hand, the Newlands kimberlites host an exceptionally large number (and variety) of garnets as xenocrysts. The lack of xenoliths and the amount of highly resistant xenocrysts suggest that the Newlands kimberlite parental melts were exceptionally rich in a carbonatitic volatile component (e.g., Giuliani et al., 2020). A carbonatitic melt in transit through the mantle lithosphere is highly efficient in assimilating mantle minerals, especially orthopyroxene. Giuliani et al. (2020) show that up to 15% (by mass) of orthopyroxene can be dissolved in kimberlites to generate the spectrum of kimberlite melt compositions that reaches the upper crust, and even higher amounts of orthopyroxene can be dissolved if the carbonatite-dominant melt assimilates bulk peridotite material in the deeper lithosphere. These conclusions are also in agreement with the experimental data in Chepurov et al. (2013), who correlate the absence of orthopyroxene as macrocryst in kimberlite to its interaction with hydrous kimberlite melts. This will move the melt towards group II orangeites. A continued production of a CO_2-rich fluid will increase abruptly the rising velocity, accompanied by decompression and changing the geochemical compositions of the preserved mantle minerals (Giuliani et al., 2020, and references therein).

Due to its complex chemical composition and expanded P-T stability field, garnet can reveal the processes operating throughout almost the entire thickness of the sub-cratonic lithospheric mantle.

The Newlands garnets present a group of Cr-pyropes (type 4), with ultra-depleted CaO (<0.7 wt%) and very-low incompatible-trace-element contents (Fig. 7g and S-3) equilibrated in the deep lithosphere along the cold geotherm at pressures of ~4.5 GPa (Fig. 9a). This indicates that the Newlands pipes sampled fragments from the ancient (Early Archean?) pre-metasomatized cratonic harzburgites, forming Cr-pyrope type 4.

The extremely negative slopes for M-HREE patterns (especially Sm to Ho) of Cr-pyrope type 4 are difficult to explain as a simple residuum of a high degree of melting or as peridotite reactions with metasomatic fluids. Based on experimental and numerical modelling (Brey and Kohler, 1990; Tomlinson and Holland, 2021, and references therein), such (rare) garnets should coexist in chemical and textural equilibrium with highly refractory olivine ($Fo_{95.4}$) at 5 GPa (Fig. 9b). However, such mineral compositions were rarely encountered in global samples of depleted lithospheric mantle, i.e., harzburgites, or as diamond inclusion suites (Walsh et al., 2023). Moreover, applying the simple batch melting formulation, even with a melting regime ~250 °C higher than the present-day mantle melting state, such residual composition can be reached only after 40–45% melting of primordial mantle (ol 56%; opx 20; cpx 14%, gt 10%; melting parameters in Table S6), i.e., well above the complete garnet consumption (estimated ~35 melting at 4 GPa: Table S6). We therefore suggest as highly likely that the ultra-depleted subcalcic Cr-pyrope is originally exsolved by residual orthopyroxene (e.g., Gibson, 2017).

In our model, the REE contents of the hypothetical residual orthopyroxene can be obtained by 45% of batch melting of primitive mantle (McDonough and Sun, 1995). The solid residuum will be composed of ol 72% and opx 28%. By hypothesizing a subsolidus re-equilibration of REEs (Bonadiman et al., 2005;Simon et al., 2008; Sun and Liang, 2014), the new garnet (~6%, based on HREE redistribution) will form at expense of orthopyroxene, matching the Dy—Lu contents of Cr-pyrope type 4 (Fig. 10a; modelling parameters in Table S6). L-MREE (La—Tb) will be subsequently added through metasomatism. This is also in agreement with the garnet LREE/HREE ratios inferred by Pokhilenko et al. (2015) as a proxy for a metasomatic indicator. The estimated pressure for type 4 (~4.5 GPa) does not exclude the source of carbonatite-rich fluid/melt at the lithospheric/asthenospheric boundary (Walsh et al., 2023).

While clinopyroxene exsolution from mantle orthopyroxene is widely reported (Simon et al., 2008; Sun and Liang, 2014), garnet exsolutions from orthopyroxene are rarely observed in mantle rocks but are described in a lherzolite xenolith from the Monastery, Bellsbank and Frank Smith kimberlites (Dawson, 2004; Dawson and Smith, 1977). More recently, Gibson (2017) analyzed mantle xenoliths entrained in kimberlites from the southern parts of the Kaapvaal Craton and demonstrated that sub-solidus garnet exsolution occurs over an extensive depth range (2.6–5.3 GPa) in the Kaapvaal lithospheric mantle. On the basis of analyses of the exsolution textures involving garnet and sometimes clinopyroxene in mantle-derived orthopyroxenes from the Kaapvaal Craton, Gibson (2017) estimated that up to 23% in garnet volume (at Jagersfontein) formed from orthopyroxene.

5.3. Mantle metasomatism – multiple stages

The exceptionally low CaO and trace element concentrations derived from orthopyroxene exsolution make the ultra-depleted garnet readily susceptible to geochemical overprinting by Ca-rich metasomatic melts. In the proposed metasomatic model (Figs. 10, 11), we suppose that the Cr-pyrope type 4 (stage 1 of metasomatism) preserved pre-metasomatized HREEs of the extremely depleted harzburgite paragenesis, and experienced L-MREE enrichment when a carbonatite-rich fluid/melt permeated the ultra-depleted mantle, while orthopyroxene was chemically disrupted (Fig. 10a).

To test this process, we applied a simple 1-D porous flow of the plate model (Vernières et al., 1997) which reproduces the chromatographic fractionation of REE during infiltration of a LREE-enriched carbonatitic fluid/melt in an extremely depleted peridotite matrix. We assumed that the carbonatitic fluid/melt initiating the metasomatism has the composition of high-density fluids (HDF) captured by diamonds during their growth (e.g., Weiss et al., 2013). In our calculations, we used the composition of HDFs trapped in diamonds from DeBeers pools (Weiss et al., 2013).

Cr-pyrope type 3 to 1 (stages 2 to 4) formed by continuous evolving reactions from the initial carbonatitic HDF-type fluids. The effects of the latest metasomatic stages in the more surficial types 1 and 2 are responsible for the Y and Zr enrichment in Fig. S6.

Principles and parameters adopted in the modelling are illustrated in Table S6 and are summarized below:

Stage 1 (type 4 modelling): The REE pattern of Cr-pyrope type 4 is replicated if 1.5% carbonatite HDF-type fluid/melts permeate an opx (17%) + ol (77%) + gt (6%) ultra-depleted matrix, in the deep lithosphere (i.e., 5 GPa and $Fo_{95.4}$) (Figs. 9b, 10a). The very small volume of reactive melt/fluid does not modify the pre-metasomatic mantle P-T condition of 37–40 mW/m^2 of the convective regime (Figs. 9a, 10a, 11).

Stage 2 (types 3 modelling): the REE pattern of Cr-pyrope type 3 is reproduced if the garnet formed in stage 1 (type 4) continues to react with the evolved carbonatitic melt that progressively exsolves CO_2 and dissolves orthopyroxene, acquiring SiO_2, CaO, and HFSE (Zr, Hf, Ti). The most enriched type 3 garnets are modelled by reaction with a larger volume of silicate-carbonatite melt (20%, Fig. 10a). Therefore, we argue that at this stage the mantle domain becomes lherzolitic in composition with olivine estimated ~ Fo_{92} at 5 GPa; Figs. 9b, 11), forming Ca-richer garnet and possibly newly formed clinopyroxene. The P-T conditions reflect the effects of a larger volume of reacting Si-rich carbonatite melt pervading the harzburgitic matrix, recording relatively high T (1000–1070 °C) but deviating from the 40–45 mW/m^2 geotherms (4.8 GPa) towards a pseudo-adiabatic ascent (3.3 GPa) (Fig. 9a) equilibrating lherzolitic olivine ~ $Fo_{92–90}$ at 3 GPa (Fig. 9b).

The Cr-pyrope type 2 REE profiles evolved from the sinusoidal trend

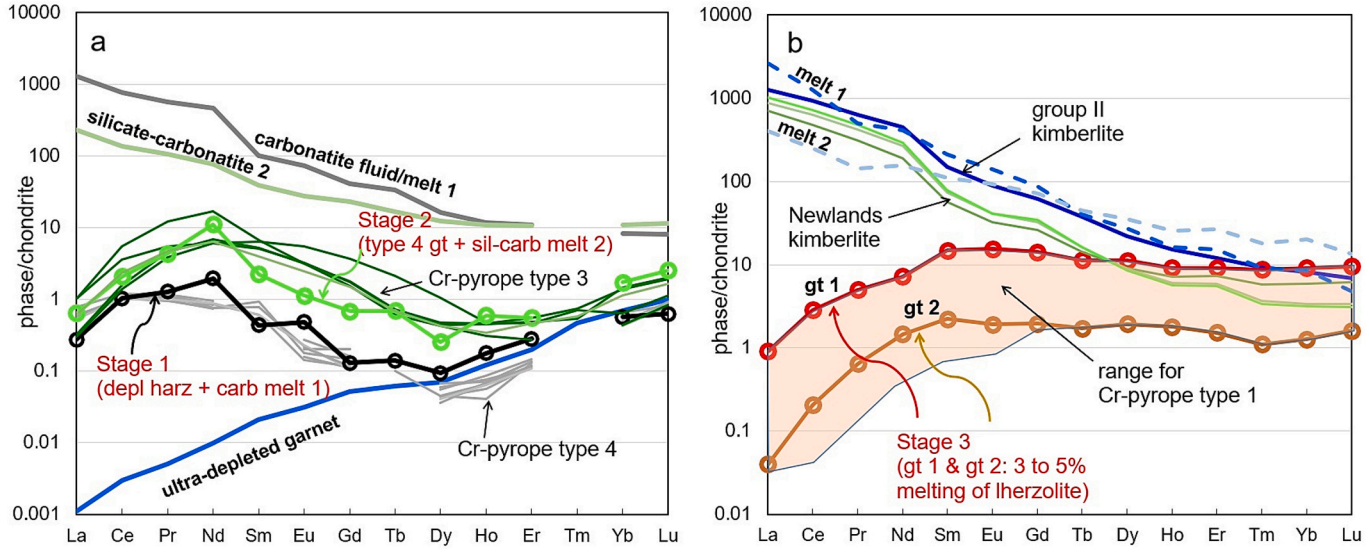


Fig. 10. Modelling of Cr-pyrope types. a) HREE of ultra-depleted Cr-pyrope type 4 (blue line) is the result of solid-state reaction of orthopyroxene (opx) from highly depleted harzburgitic mantle (ol 72% and opx 28%). The high L-MREE (compared to the ultradepleted garnet) and the sinusoidal pattern of type 4 are the result of 1.5% carbonatite fluid/melt permeating the ultra-depleted harzburgite with exsolved garnet (Stage 1 in figure). The carbonatite fluid/melt used in the model is the high-density fluids (HFD) trapped in diamonds from De Beers pools, Kimberley, South Africa (Weiss et al., 2013). At Stage 2, Cr-pyrope type 3 is matched by reaction of Cr-pyrope type 4 with a progressively more evolved carbonatitic melt (silicate-carbonatite melt 2) exsolving CO_2 and enriching in SiO_2 and CaO. The most enriched type 3 garnets are modelled by reaction with a larger volume of silicate-carbonatite melt (20%), resulting from evolution of Stage 1 (Stage 2 in figure). b) The reddish pattern defines the range for Cr-pyrope type 1 (forming at stage 3). The maximum in this range was modelled as gt 1 from 3% melting of refertilized lherzolite (melt 1, blue dashed line). Melt 1 overlaps with South African primary kimberlite group II of Becker and Le Roex (2006) (solid blue line), and with the Newlands kimberlites (green patterns, this work). The minimum in the range was modelled as gt 2 from 5% melting of lherzolite (melt 2, light blue dashed line). Melt 2 shares similarities with off-craton lithosphere in Becker and Le Roex (2006) and is not reported in fig. C1 Chondrite from McDonough and Sun (1995). (For interpretation of the references to colour in this figure legend, the reader is referred to the web version of this article.)

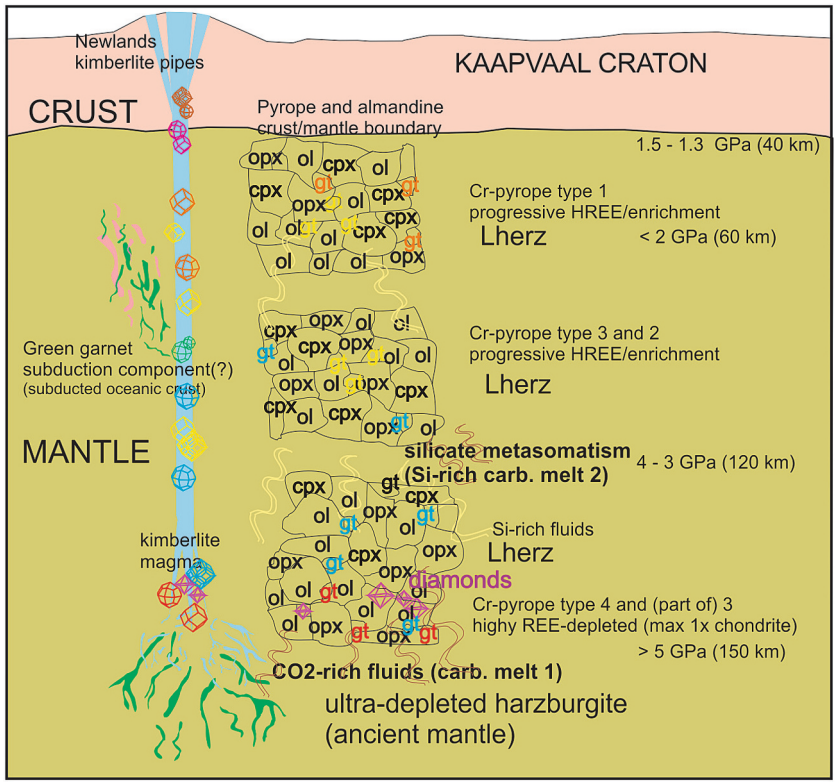


Fig. 11. Sketch cartoon with simplified representation of the proposed enrichment/metasomatic processes in the mantle sector beneath Newlands, producing transition from type 4 to type 1 Cr-pyrope. Colors of Cr-pyrope correspond to: orange = type 1, yellow = type 2, blue = type 3, red = type 4. Green = Cr-Ca-rich garnet, purple = pyrope, brown = almandine. (For interpretation of the references to colour in this figure legend, the reader is referred to the web version of this article.)

of type 3 to a humped pattern, with positive slopes from LREE to MREE and with Eu up to 17 times chondrite but with a smoother fractionated HREE pattern. This feature preludes the variably fertile REE profiles of type 1.

Stage 3 (type 1 modelling): Cr-pyrope type 1 shows positive slopes for LREE and a nearly flat profile for MREE and HREE. The progressive flattening of the M-HREEs records the approaching of equilibrium of a variably fertile (or re-fertilized) lherzolite with a primary kimberlite melt (e.g., Griffin et al., 1999; Becker and Le Roex, 2006). We tested this hypothesis, assuming that at this stage we reach a fertile 'new' lherzolitic composition (by a re-fertilization process), which is stable along the 40–45 mW/m^2 geotherms (3.5–4.3 GPa) in equilibrium with a primary kimberlite melt and olivine ~ Fo_{90} (Figs. 9a, b, 11). The relatively large REE range (La_N: bdl-0.91; Yb_N: 1.34–9.54) of Cr-pyrope type 1 (Stage 3 in Fig. 10b) is coherent with a fertile lherzolite matrix in equilibrium with silicate melts forming in the pressure range of ~3.5–2.0 GPa (gt 1 and gt 2, respectively, in Fig. 10b; Grove et al., 2013) by melting of fertile lherzolite, and forming primary silicate melts (melt 1 and melt 2 in Fig. 10b). Melt 1, in equilibrium with the modelled lherzolite garnets, overlaps the REE contents of the South African primary kimberlite group II of Becker and Le Roex (2006), and mimics the REE profiles of the Newlands kimberlites (Fig. 10b). Melt 2, calculated in equilibrium with the most depleted type 1 garnet, has a higher MREE and lower LREE profile, similar to melt formed in shallow off-craton lithospheric mantle (Becker and Le Roex, 2006).

The $(La/Yb)_N$ vs Ti/Eu diagram (Coltorti et al., 1999) adapted for Newlands Cr-pyropes clearly visualizes the three main steps of metasomatism. The original diagram has strong discriminating power for metasomatic clinopyroxenes or bulk rocks (Coltorti et al., 1999), due to the partitioning behavior of La, Eu, Ti and Yb between carbonatite and silicate melts and clinopyroxene. La is incompatible in both clinopyroxene and garnet for carbonatitic and silicate mantle-derived melts. $Kd_{La}^{garnet/melt}$ is approximately one order of magnitude lower than $Kd_{La}^{cpx/melt}$ ($Kd_{La}^{garnet/carb\ and\ carbsilicate}$ ~ 0.005–0.04; $Kd_{La}^{garnet/carb\ and\ carbsilicate}$ ~ 0.015–0.15) whereas Yb is compatible in garnet and slightly incompatible in clinopyroxene ($Kd_{Yb}^{garnet/carb\ and\ carbsilicate}$ ~ 2–3; $Kd_{Yb}^{cpx/carb\ and\ carbsilicate}$ ~ 0.2–0.6) (e.g., Dasgupta et al., 2009; Keshav et al., 2005; Girnis et al., 2013). Although the absolute partition coefficients differ between garnet and clinopyroxene, the relative behavior of these elements follows the same first-order direction. Therefore, the combined $(La/Yb)_N$ vs Ti/Eu systematics can provide broadly comparable information to that obtained from clinopyroxene, although with greater interpretative uncertainty. Despite the uncertainties mentioned above, we noticed that the distribution of metasomatized Cr-pyrope in this diagram supports the proposed evolutionary model.

Cr-pyrope type 4 formed in diamond stability fields by ultradepleted peridotite interacting with LREE enriched carbonatite HDF-type fluid/melts (Fig. 12). Such melt changes rapidly in composition dissolving matrix silicates and basaltic components (i.e. Ti and Al) and forming, without discontinuity, type 3 and type 2 as the metasomatic reactions proceed (Fig. 12). It is interesting to note that a group of Cr-diopsides falls in the same metasomatic field of Ca-poor (CaO < 1 wt%) Cr-pyrope type 4 (Fig. 12), and they record the same range of equilibration (~4.5 GPa, T ~ 850–1000 °C) Cr-pyrope type 4 (Fig. 9a). This suggests that also Cr-diopside is a product of stage 1 metasomatism, due to the occurred Ca-saturated system, and its capacity to accommodate LREE more easily with respect to garnet (Kd_{LREE} cpx/carb two orders of magnitude larger than Kd_{LREE} gt /carb; Walsh et al., 2023, and references therein).

5.4. Evidence of crustal recycling?

5.4.1. Stable isotopes

Carbon and S isotopes were measured on grains of almandine, pyrope, and Cr-pyrope. Stereoscopic observations of the grains used for measurements reveal the lack of evident fractures and zoning, suggesting limited effects of contamination by the kimberlite or alteration by low-pressure fluid circulation (Giuliani et al., 2014). The isotopic measurements are difficult to interpret and can be speculative because both carbon and sulfur are not considered possible vicariants in garnet, but they can be present as fluid or solid microinclusions. Carbon content in single grains was confirmed to be very low (~0.065 wt%). Therefore, our pioneering approach suggests great caution when interpreting the results. On top of that, low-temperature processes can affect both carbon and sulfur fractions, as well as their final contents (Fitzpayne et al., 2021; Giuliani et al., 2014; Ionov et al., 2024). Thus, the data are very preliminary, and provide results that will need to be confirmed by more rigorous in-situ isotopic studies (for example, using SIMS/NanoSIMS). Results are in Table S4.

Carbon extracted at $T > 800$ °C is characterized by $\delta^{13}C$ from −24‰

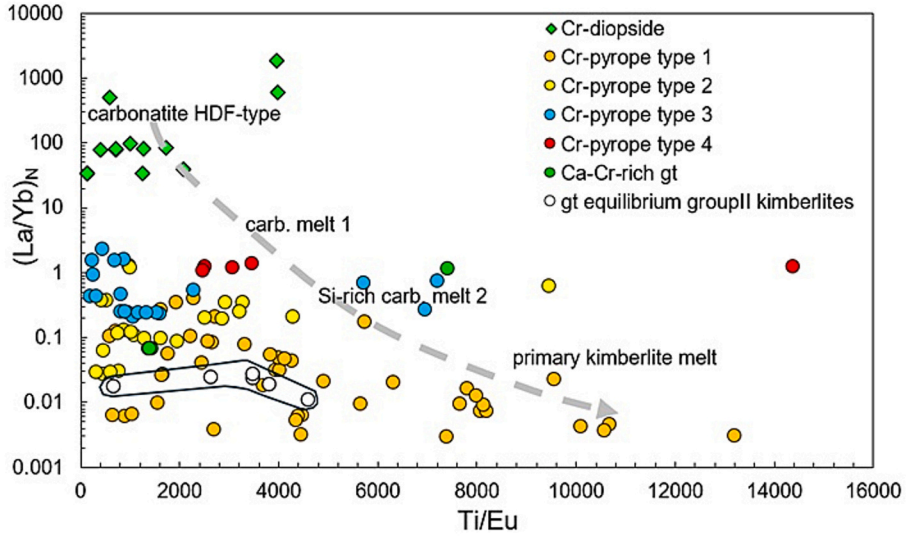


Fig. 12. Chondrite-normalized (La/Yb)N vs Ti/Eu diagram (after Coltorti et al., 1999) for Newlands Cr-pyrope, Ca–Cr-rich garnet, and Cr-diopside illustrating the transition from carbonatite/CO_2-rich-fluid metasomatism to silicate-melt metasomatism. High to very high Ti/Eu ratios show remarkable effects of host rock interaction. REE for garnet in equilibrium with Group II kimberlite are calculated using Kd from Girnis et al. (2013) and Adam and Green (2006). Ti concentrations used in the ratio are expressed in ppm. (For interpretation of the references to colour in this figure legend, the reader is referred to the web version of this article.)

(Cr-pyrope) to −17‰ (almandine). The small value range is comparable to that obtained in kimberlitic mantle xenoliths and interpreted as primary dissolved carbon and organic material present on cracks in the xenoliths (Pineau and Javoy, 1983) or as surface contamination (Mattey et al., 1984).

By analyzing cleaned single grains, we removed potential grain surface alteration and reduced the effects of surface contamination, and, therefore, we infer that these values may represent the original isotopic composition. Based on the observation that altered mafic-ultramafic oceanic crust contains carbonates with $\delta^{13}C$ values as low as −24‰, we argue that the isotopic signature may reflect the involvement of crustal material at various levels of the mantle column. Li et al. (2019) provide the same explanation for similar C isotopes in diamonds of the Kaapvaal Craton (Jagersfontein and Monastery, with $\delta^{13}C = -18$ to −23‰), implying that an altered ocean crust (AOC) instead of sediments is the key carrier of crustal carbon into the deep mantle.

Sulfur contents in the analyzed garnets are close to detection limits. Therefore, the $\delta^{34}S$ values of ca. -3‰, recorded for both mantle and crustal grains, need to be validated by further analyses.

Unfortunately, only limited S isotopic data are available for kimberlites and sub-continental lithospheric mantle sources. A wider range of $\delta^{34}S$ values at −5.9 to −1.4‰, compared with our results, was measured in single sulfides and whole rock in metasomatized mantle xenoliths from Bultfontein kimberlites (Giuliani et al., 2016). The authors interpret these values as an indication of metasomatic fluids active beneath Kimberley at ~180 Ma and 90–80 Ma and sourced from a reservoir with limited S isotope variations. The low $\delta^{34}S$ in the Bultfontein xenoliths suggests that the fluid source was probably located in the asthenospheric mantle, contained recycled crustal S, and that this signature was largely unmodified during ascent through the lithospheric mantle (Giuliani et al., 2016; Ionov et al., 2024).

More data are needed to constrain the isotopic meaning, but we can tentatively suggest that $\delta^{13}C$ and $\delta^{34}S$ of mantle and crustal Newlands garnets show inference of recycled crustal components (altered oceanic crust + sediments) for the entire spectrum of metasomatic melts acting in time along the mantle column.

5.4.2. Redox conditions

An important parameter that influences the spectrum of geochemical processes affecting a fluid or melt's ability to migrate within an ambient peridotite mantle (i.e., carbon migrating as carbonate or being stored as graphite or diamond) is the oxidation state. This is usually determined by the bulk Fe^{3+}/Fe_{tot} ratio through ferric-ferrous equilibria involving mantle silicates and oxides. The Fe^{3+} contents will be continually altered through interactions with migrating melts or fluids, or by the juxtaposition of rock domains with different fO_2 levels (e.g., Bonadiman et al., 2021; Stagno and Aulbach, 2022; Woodland et al., 2018). The absence of discrete peridotite xenoliths in Newlands prevents applying oxy-geobarometers based on phase equilibria for calculating oxygen fugacity (fO_2) (e.g., Luth and Canil, 1993), but garnet trace chemistry indeed provides important information.

Vanadium and Sc are lithophile elements with similar mildly incompatible behavior and partitioning in garnet ($Kd_V^{gt/kim}$ 1.0–5.0; $Kd_{Sc}^{gt/kim}$ 1.8–5.0, Girnis et al., 2013), but only V is multivalent in nature (V^{2+}, V^{3+}, V^{4+}, V^{5+}). Scandium, instead, can be added to or removed from garnet depending only on the elemental concentration of the metasomatic melt relative to that dictated by its partition coefficient for equilibrium with peridotite garnet. This means that the V concentration or V/Sc ratio in garnets could serve as a proxy for the oxidation state of the original peridotite matrix (Woodland et al., 2018).

Moreover, it has been suggested that V concentrations in peridotites are less affected by late-stage alteration processes than Fe^{3+}/Fe^{2+} and therefore better preserve information about the oxidation state during peridotite/metasomatic melt interactions at depth (Cottrell et al., 2025; Fux et al., 2025; Woodland et al., 2018). Metasomatic interactions seem to have a direct influence on V concentrations in garnet, as was demonstrated for clinopyroxene (Cottrell et al., 2025; Woodland et al., 2018). This occurs when the fO_2 of the agent is different from the initial mantle conditions.

Newlands garnet population seems to reflect the original redox conditions during the various stages of metasomatism that gradually changed the carbonatitic HDF-type fluids in patent kimberlite melt (Figs. 11, 12). Cr-pyrope type 3, and to a lesser extent type 2, modelled as forming through the reaction of harzburgite with large volumes of silicate-carbonatite melt (Fig. 10a) are, among the Cr-pyrope types, the richest in Sc and V (Fig. 13a). Considering that metasomatism is usually associated with oxidation (Foley, 2011), modification of V content is also correlated with Fe^{3+}/Fe_{tot}, although the higher oxidation of types 3 and 2 is not always visible due to the Fe^{3+} calculation by stoichiometry (Fig. 13b). Cr-pyrope type 1, showing a well-equilibrated lherzolite REE pattern (also known as 'normal' profile, Fig. 7d; Hoal et al., 1994), is relatively depleted in Sc and V, with relatively low Fe^{3+}/Fe_{tot}, suggesting an equilibrium with less metasomatized and fertile peridotite. Instead, based on formula stoichiometry, Cr-pyrope type 4, modelled as subsolidus reaction products of extremely depleted orthopyroxene, does not account for Fe^{3+} (Table S2). This likely happens because type 4 garnet experienced initial metasomatism by deep carbonatitic (diamond-forming) HDF-type fluids (Figs. 10a, 11, 12), preventing the oxidation of the peridotitic mantle (Mershon et al., 2025; Weiss et al., 2013), and the presence of ferric iron in garnet. This is also observed in garnet from cpx-free harzburgites in various Kaapvaal mantle xenoliths (i.e., Finsch harzburgites, Lazarov et al., 2009).

We cannot quantify the redox states of the mantle-forming Newlands garnet population, and garnet can crystallize in different redox conditions, from H_2O-rich to oxygenated hydrocarbon-rich (e.g., Chepurov et al., 2025; Sobolev et al., 2019). However, the majority of Newlands Cr-pyrope has Fe^{3+}/Fe_{tot} ratio (0.02–0.08) in the same range of values as garnets from variably depleted and metasomatized Kaapvaal peridotite (data collection from Stagno et al., 2013). Limiting the comparison to the same P-T range and Fe^{3+}/Fet_{ot} ratio of the Newlands peridotite garnets, the estimates of fO_2 reported relative to fayalite-magnetite-quartz oxygen buffer equilibrium ($\Delta \log fO_2$ [FMQ]) are in the range of −4.5 to −2.5 log units. Taking into account the Fe^{3+}/Fe_{tot}-V relationships, we can only argue that the less metasomatized lherzolitic type 1 garnet could record the lowest fO_2 ($\Delta \log fO_2$ towards −4.5); whereas the highly metasomatized type 3 (and type 2) garnets could reflect a highly oxidized ambient peridotite mantle ($\Delta \log fO_2$ towards −2.5) without apparent correlation with pressure (Fig. 10a).

In addition to Fe and V, U is also a redox-sensitive element with multiple oxidation states. Uranium in garnet is highly incompatible ($Kd_U^{gt/kim}$: ~10^{-3}–10^{-4}; Adam and Green, 2006; Keshav et al., 2020). Vanadium is positively correlated with U (Fig. 13c). This correlation cannot be attributed to the interaction of garnet grains with host magmas. Newlands kimberlites and calculated garnet in equilibrium with these compositions clearly have U, V, and Sc compositional ranges completely different from those of Newlands mantle garnets (Fig. 13c). It is confirmed that Cr-pyrope type 3 and type 2 formed by a highly oxidized ambient peridotite. Moreover, since V and U have opposite geochemical behavior, the positive correlation suggests that U concentration is low to very low in well-equilibrated mantle garnets (i.e. 'normal' lherzolitic Cr-pyrope type 1), but can also be incorporated in this mineral by metasomatism. Finally, it is clear that also the extremely depleted Cr-pyrope type 4 experienced metasomatism by interaction with fluid/melts geochemically similar to those forming types 1–3 (Fig. 13a, c). We can thus argue the presence of V and U in the metasomatic fluid/melts. These elements may be indicators of submarine organic activity recorded by marine sediments, such as bituminous black shales. In these environments, V can form organometallic complexes through sub-anoxic or anoxic reactions (Huang et al., 2015). Meanwhile, U commonly forms phosphates during marine sedimentation (Abshire et al., 2020). These compounds are very resistant and act as excellent carriers for transporting U and V into the deep mantle via subduction

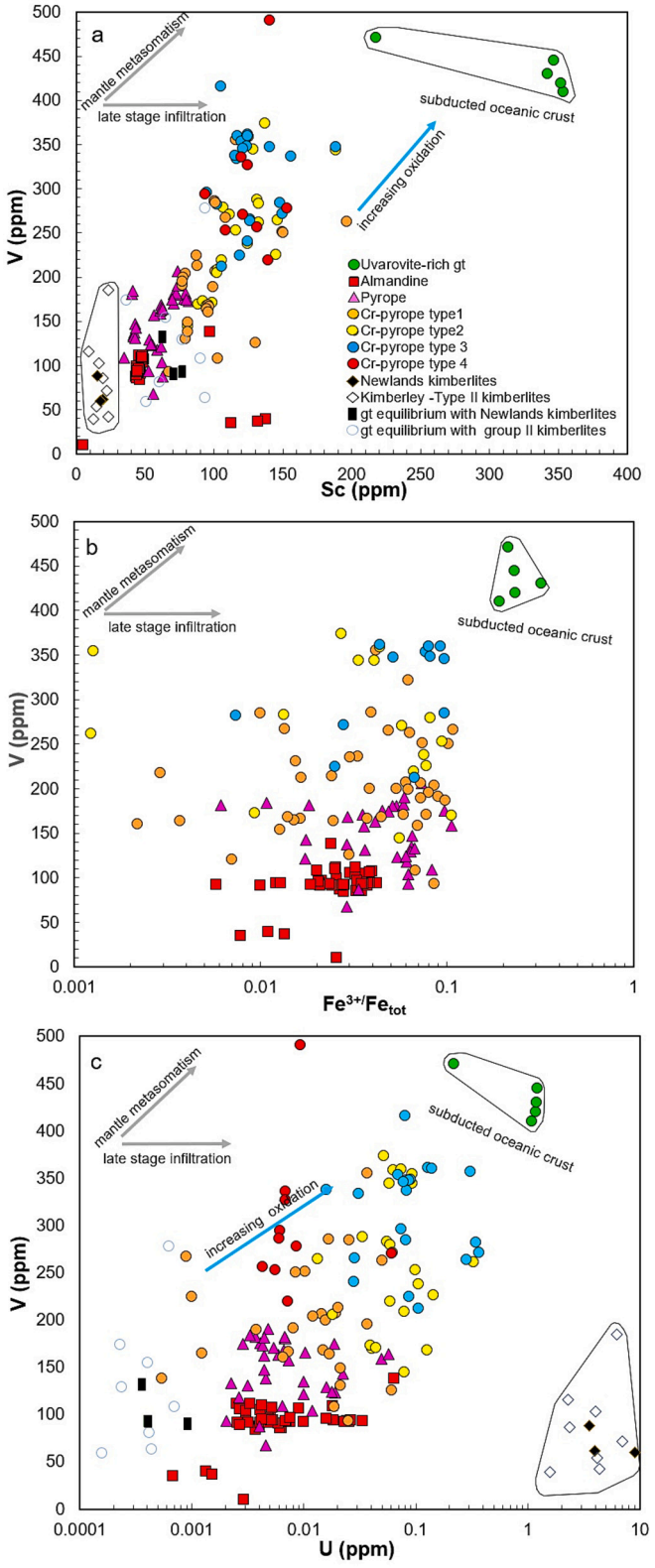


Fig. 13. Variations of V vs Sc (a), V vs Fe^{3+}/Fe_{tot} (b), and V vs U (c) for garnets from Newlands kimberlite. Composition of Newlands and Kaapvaal kimberlites (diamonds) is also reported. Garnet in equilibrium with Group II kimberlites (a, c) is calculated using Kd from Girnis et al. (2013) for V and Sc, and Adam and Green (2006) for U. (For interpretation of the references to colour in this figure legend, the reader is referred to the web version of this article.)

(Abshire et al., 2020). Therefore, we suggest that the carbonatite HDF-type fluids and the subsequent geochemical and redox modification due to a continuous reaction with the surrounding mantle peridotite reflect the contribution of recycled oceanic crust components.

The trace-element contents and REE profiles of the almandine xenocrysts (Fig. 7) are consistent with those of garnets from mafic granulites, including orthopyroxene-bearing garnet clinopyroxenites and garnet websterites, interpreted as metamorphosed lower-crustal samples and reported as xenoliths in kimberlites emplaced near the southern margin of the Kaapvaal Craton (Le Roex et al., 2020). Moreover, the garnet pyroxenites and granulites investigated by Le Roex et al. (2020) yielded equilibration temperatures of 686–835 °C, based on Fe—Mg exchange between clinopyroxene and garnet, and pressure estimates of 1.3–1.7 GPa. These conditions are strictly consistent with our estimates of 823–849 °C and 1.3–1.4 GPa, which are based on independent equilibria involving pyrope–almandine solid solutions and Ti-in-garnet thermometry for garnet coexisting with orthopyroxene and quartz.

Therefore, the Newlands almandine and pyrope xenocrysts might represent fragments of original mafic granulites that re-equilibrated during crustal shortening and thickening associated with the collision of the Namaqua–Natal Belt with the Kaapvaal Craton at ca. 1.1–1.2 Ga (Le Roex et al., 2020). These results are also supported by the first, preliminary C and S isotopic ratios.

5.5. Cr-Ca-rich (green) garnet

Close to Newlands, the presence of green garnets in Phanerozoic kimberlites has been documented at the Kampfersdam kimberlite, Kimberley (Schulze, 1989). Besides these findings, Cr-Ca-rich garnet was documented only in Yakutia, Venezuela, and Canada (Nosova et al., 2025; Sablukova et al., 2012, and references therein). The Ca–Cr-rich garnets are rare in the mantle because they require the simultaneous availability of high Ca and high Cr, in a specific chemical environment in which both Ca and Cr are available to enter the garnet structure. Moreover, Ca and Cr are negatively correlated in whole-rock residues. In the upper mantle domain, Ca is mainly hosted by clinopyroxene, whereas Cr is commonly partitioned into spinel or chromite. Therefore, garnet compositions that are simultaneously enriched in Ca and Cr will reflect domains where Ca availability, high Cr activity, garnet stability, and metasomatic reaction processes coincide (Gao et al., 2025). The stability of this type of garnet in the lithosphere is supported by numerous experimental studies (Gréaux and Yamada, 2019). Their origin is highly debated, variably attributed to mantle melting at depth, H_2O-CO-fluid metasomatism on a mantle protolith, metamorphism of serpentinites in collisional zones, and derivation from crustal material (e.g., Clarke and Carswell, 1977; Schulze, 1989; Sobolev et al., 2004). The Cr-Ca-rich garnets at Newlands show high Cr and extreme Ca content (CaO range: 18.7–21.3 wt%). They retain a mantle signature (high Mg#: 0.80–0.83), within the same stability field of Cr-pyrope types 2 and 1, with pressure of ca. 2.5 GPa and T at 980–1010 °C (in agreement with Sablukova et al., 2012; P: 2.5–2.7 GPa; T: 1019–1106°C), in equilibrium with a metasomatized lherzolitic mantle. However, they differ from the other Newlands mantle garnets in having anomalously high Fe^{3+}/Fe_{tot} ratios from stoichiometry, and the highest concentration of V and U of the entire garnet population (Figs. 13b, c). This suggests that they formed in a highly metasomatized ambient peridotite mantle with probably $\Delta \log fO_2$ [FMQ] < -2.5 with a relevant contribution of recycled oceanic components (Fig. 11; Abshire et al., 2020). The P-T conditions for the Cr-Ca-rich garnet, far from the diamond stability field, suggest that at Newlands, Ca-Cr-rich green garnet (uvarovite-rich component) is not indicative of diamond fertility. However, Ca-Cr-rich garnet is often found as microinclusions in diamonds (e.g., Sobolev et al., 2004; Stachel et al., 2022). We suggest that the peculiar flat REE pattern of Cr-Ca-rich garnet at Newlands (with no Eu anomaly, Fig. 7a), could be a topomorphic feature of green garnet crystallizing outside the diamond stability field. Oxygen isotopic composition of

green garnets ($\delta^{18}O = 4.05–4.25‰$) from a polygranular sample with 60 and 90% of garnet in an ol + opx altered matrix (Sablukova et al., 2012) differs drastically from the mantle values ($\delta^{18}O = 5.5\pm0.4‰$; Mattey et al., 1994), overlapping the values obtained by the 3.27 Ga komatiites of the Weltevreden Formation in the Barberton Greenstone Belt in Southern Africa (Ouyang et al., 2024). These $\delta^{18}O$ values are explained by recycling of the altered oceanic crust into the deep mantle, arguably by subduction, which started 3.3 billion years ago, and is responsible for the deep mantle heterogeneity in early Earth (Ouyang et al., 2024). Therefore, combining the various lines of evidence, we suggest that green garnet at Newlands is formed by reaction of peridotite with melted subducted oceanic crust entrained randomly in the upwelling mantle domain, probably well before the entrapment in the host kimberlite (e.g., Abshire et al., 2020). Not much material was available for this study, and further collection of Newlands green garnets will be devoted to a more in-depth study of the crystallochemical and isotopic characteristics of this uncommon group of mantle garnets.

5.6. Diamond fertility at Newlands

The geochemistry of Cr-rich garnet and the inferred P-T constraints represent a powerful tool for diamond exploration, due to the garnet's capability of tracking back diamond-fertile portions of the mantle (e.g., Grütter et al., 2004). The compilation and processing of a large geochemical dataset of garnet in xenoliths, microxenoliths, and inclusions in diamonds provided classification schemes based on major element distribution that highlight grains crystallized in the diamond stability field with compositional association with diamonds. Among these diagrams, the one proposed by (Fig. 8; Grütter et al., 2004) suggests a co-existence of diamond crystallization with Ca-undersaturated garnet in ultra-depleted harzburgite.

Diamond formation in a harzburgitic host mainly occurred during the Archean (e.g., Gurney et al., 2010). In these ancient and depleted mantle sources, REE patterns usually display a sinusoidal trend with low MREEs. In exceptionally ultra-depleted garnets, normalized values can plot below 1 chondrite (Gibson, 2017; Griffin et al., 1999). At Newlands, this happens for Cr-pyrope type 4 and part of type 3 (Fig. 7). The highest calculated equilibration pressures, i.e., between 4.5 and 4.9 GPa, plot these Cr-pyropes in the diamond field, or at the transition between diamond and graphite (Fig. 9a). Moreover, Cr-pyrope type 4, with undetectable ferric iron, and likely subjected to initial metasomatism by deep carbonatitic (diamond-forming) HDF-type fluids (Figs. 10, 11, 12), is in equilibrium with a surrounding peridotitic mantle with relatively low redox conditions (Fig. 12). This is favourable for diamonds to form and be preserved alongside it. Therefore, at Newlands, the most diamond-rich kimberlite pipes are likely those containing high concentrations of Cr-pyrope type 4 (Fig. 12).

6. Conclusions

The diamondiferous Newlands kimberlite (South Africa), dated at ~144 Ma, is classified as part of the group II kimberlites (orangeites). The pipe object of this study is characterized by the scarcity of discrete sensu stricto mantle xenoliths and by the presence of a large variety of garnets. Cr-diopside is rare. The spectrum of mantle-derived Cr-pyrope allowed us to reconstruct the dynamic evolution of the mantle column.

Cr-pyrope type 4, with ultra-depleted CaO (<0.7 wt%), very-low incompatible-trace-element contents and M-HREE (avg $Dy_N = 0.05$; avg. $Yb_N = 0.53$), originally formed by chemical exsolution of high residual orthopyroxene (45% melting of primary mantle), and testifies to a pre-metasomatized highly residual harzburgitic mantle at a very initial metasomatic stage (avg $Ce_N = 1.44$). The inferred depth between 145 and 155 km (~5 GPa), the relative depletion of the redox sensitive elements (Fe, V and U) and the nature of the modelled initial melt, suggest kimberlite hosting Cr-pyrope type 4 being in equilibrium with diamonds. Cr-pyrope is also a product of stage 1 metasomatism, due to the occurred Ca saturated system, and its capacity to accommodate LREE more easily with respect to garnet.

Cr-pyrope types 3 and 2 testify to the dynamic evolution of the Kaapvaal lithospheric mantle, where the continuum of melt/rock interaction changed the nature of metasomatic melts in time and space. The melt progressively became more oxidized with more evident contribution of recycled oceanic components. The ambient peridotite mantle progressively moved to a more lherzolitic composition, forming Ca-richer garnet with high concentration of V, U and Fe^{3+}, and possibly newly formed clinopyroxene. At a shallower mantle level, a fertile (re-fertilized) lherzolite matrix in equilibrium with silicate formed by 3–5% of lherzolite melting in the pressure range of ~3.5–2.0 GPa, matching the compositional range of Cr-pyrope type 1. Cr-pyrope type 1 represents well-equilibrated less metasomatized, re-fertilized lherzolitic mantle. The resulting melts mimic the REE profile of modelled South African primary group II kimberlite.

A different blob of re-fertilized lherzolite in the same stability field of Cr-pyrope types 2 and 1 contains Cr-Ca-rich (green) garnet with anomalously high V, Fe^{3+}, and U concentrations. These features suggest that green garnets formed by reaction of peridotite with melted subducted oceanic crust entrained randomly in the upwelling mantle domain, probably well before the entrapment in the host kimberlite. The co-existence of Cr-Ca-rich garnet and Cr-pyrope also suggests the juxtaposing fragments of re-fertilized mantle domains formed by metasomatic melts assimilating a larger contribution of recycled oceanic crust.

The presence of pyrope and almandine marks the mantle/crust boundary at ~1.3–1.5 GPa (35–40 km depth), which is in agreement with the Ps Moho conversions calculated in a neighboring area, and with the presence of garnet pyroxenites and garnet granulite xenoliths from kimberlites emplaced in the southern margin of the Kaapvaal Craton.

As much as the results can be debatable, the first C—S isotopic data performed on single garnets with mantle and crustal affinity (Cr-pyrope, pyrope and almandine) point towards the possible inference of recycled crust (altered oceanic crust + sediments) for the entire spectrum of metasomatic melts acting along the mantle column.

To conclude, the complexity of geochemical relationships and P-T variations discussed here confirms that it is possible to extrapolate the nature and composition of lithospheric mantle portions from the geochemistry of the entrapped population of garnet xenocrysts.

Supplementary data to this article can be found online at https://doi.org/10.1016/j.lithos.2026.108742.

CRediT authorship contribution statement

C. Bonadiman: Writing – review & editing, Writing – original draft, Supervision, Methodology, Investigation, Conceptualization. **L. Milani:** Writing – review & editing, Writing – original draft, Supervision, Resources, Methodology, Investigation, Funding acquisition, Conceptualization. **R. Tassinari:** Writing – review & editing, Validation, Supervision, Methodology, Formal analysis, Data curation. **N. Lenhardt:** Writing – review & editing, Writing – original draft, Resources, Investigation, Formal analysis, Data curation. **P.W.J. Delport:** Writing – review & editing, Methodology, Formal analysis, Data curation. **L. Rowe:** Writing – review & editing, Methodology, Formal analysis, Data curation.

Declaration of competing interest

The authors declare the following financial interests/personal relationships which may be considered as potential competing interests: Lorenzo Milani reports financial support was provided by Research, Education and Investment Fund (REI Fund) of the Geological Society of South Africa (GSSA). Lorenzo Milani reports a relationship with Research, Education and Investment Fund (REI Fund) of the Geological Society of South Africa (GSSA) that includes: funding grants. If there are

other authors, they declare that they have no known competing financial interests or personal relationships that could have appeared to influence the work reported in this paper.

Acknowledgements

We thank Mr. Christo Synman, director of the Newlands kimberlite mine, for kindly allowing access and sample collection at the mine. Appreciation goes to the Research, Education and Investment Fund (REI Fund) of the Geological Society of South Africa (GSSA), for supporting the costs of the XRF and EPMA analyses and to Ms. Elizabeth Wessels, who collected these data as part of her Honours degree at the University of Pretoria. We are grateful to Dr. Christian Reinke, Dr. Anna Molekwa, and Dr. Henriette Ueckermann (University of Johannesburg) for the support provided during the EPMA and LA-ICP-MS analyses. Xin Zhong is also acknowledged for helpful discussions on the geo-thermobarometric application of zircon inclusions in garnet. We thank the 'Visiting Professor Programme' at the University of Pretoria for fostering the international collaboration that allowed the research paper.

References

Abshire, M.L., Contribre, M.L., Romaniello, S.J., Kuzminov, A.M., Cofrancesco, J., Severmann, S., Riedinger, N., 2020. Uranium isotopes as a proxy for primary depositional redox conditions in organic-rich marine systems. Earth Planet. Sci. Lett. 529, 115878. https://doi.org/10.1016/j.epsl.2019.115878.

Adam, J., Green, T.H., 2006. Trace element partitioning between mica- and amphibole-bearing garnet lherzolite and hydrous basanitic melt: 1. experimental results and the investigation of controls on partitioning behaviour. Contrib. Mineral. Petrol. 152, 1–17.

Anders, E., Grevesse, N., 1989. The abundances of the elements: meteoritic and solar. Geochim. Cosmochim. Acta 53, 197–214.

Becker, M., Le Roex, A.P., 2006. Geochemistry of south African on- and off-craton, group I and group II kimberlites: petrogenesis and source region evolution. J. Petrol. 47, 673–703. https://doi.org/10.1093/petrology/egi089.

Bonadiman, C., Beccaluva, L., Coltorti, M., Siena, F., 2005. Kimberlite-like metasomatism and 'garnet signature' in spinel-peridotite xenoliths from Sal, Cape Verde Archipelago: relics of a subcontinental mantle domain within the Atlantic oceanic lithosphere? J. Petrol. 46, 2465–2493.

Bonadiman, C., Brombin, V., Andreozzi, G.B., Benna, P., Coltorti, M., Curetti, N., Faccini, B., Merli, M., Pelorosso, B., Stagno, V., Tesauro, M., Pavese, A., 2021. Phlogopite-pargasite coexistence in an oxygen reduced spinel-peridotite ambient. Sci. Rep. 11, 11829. https://doi.org/10.1038/s41598-021-90844-w.

Brey, G.P., Kohler, T., 1990. Geothermobarometry in four-phase lherzolites II, New thermobarometers, and practical assessment of existing their barometers. J. Petrol. 31, 1353–1378. https://doi.org/10.1093/petrology/31.6.1353.

Canil, D., 1999. The Ni-in-garnet geothermometer: calibration at natural abundances. Contrib. Mineral. Petrol. 136, 240–246.

Celli, N.L., Lebdev, S., Schaeffer, A.J., Gaina, C., 2020. African cratonic lithosphere carved by mantle plumes. Nat. Commun. 11, 92. https://doi.org/10.1038/s41467-019-13871-2.

Chepurov, A.I., Zhimulev, E.I., Agafonov, L.V., Sonin, V.M., Chepurov, A.A., Tomilenko, A.A., 2013. The stability of ortho- and clinopyroxenes, olivine, and garnet in kimberlitic magma. Russ. Geol. Geophys. 54, 406–415. https://doi.org/10.1016/j.rgg.2013.03.004.

Chepurov, A.A., Tomilenko, A.A., Lin, V.V., Sonin, V.M., Zhimulev, E.I., Bul'bak, T.A., Chepurov, A.I., Pokhilenko, N.P., 2025. The component composition of fluid phase during crystallization of subcalcic chromium garnet at high pressure. Dokl. Earth Sci. 522, 25.

Clarke, D.B., Carswell, D.A., 1977. Green garnets from the Newlands Kimberlite, Cape Province, South Africa. Earth Planet. Sci. Lett. 34, 30–38.

Coltorti, M., Bonadiman, C., Hinton, R.W., Siena, F., Upton, B.G.J., 1999. Carbonatite metasomatism of the oceanic upper mantle: evidence from clinopyroxenes and glasses in ultramafic xenoliths of Grande Comore, Indian Ocean. J. Petrol. 40 (1), 133–165. https://doi.org/10.1093/petroj/40.1.133.

Cottrell, E., Canil, D., Langmuir, C., Katy, A., Evans, K.A., Gaillard, F., 2025. Earth's past and present mantle oxygen fugacity. Nat. Rev. Earth Environ. 6, 728–746. https://doi.org/10.1038/s43017-025-00735-1.

Dasgupta, R., Hirschmann, M.M., McDonough, W.F., Spiegelman, M., Withers, A.C., 2009. Trace element partitioning between garnet lherzolite and carbonatite at 6.6 and 8.6 GPa with applications to the geochemistry of the mantle and of mantle-derived melts. Chem. Geol. 262, 57–77. https://doi.org/10.1016/j.chemgeo.2009.02.004.

Daniels, L.R.M., Richardson, R.H., Menzies, A.H., de Bruin, D., Gurney, J.J., 1995. Diamondiferous garnet macrocrysts in the Newlands kimberlite, South Africa – Rosetta stones from the Kaapvaal Craton Keel. In: Proceedings of the 6th International Kimberlite Conference, Novosibirsk, pp. 121–123. Doi:10.29173/ikc1803.

Dawson, J.B., 2004. A fertile harzburgite garnet lherzolite transition: possible inferences for the roles of strain and metasomatism in upper mantle peridotites. Lithos 77, 553–569.

Dawson, J.B., Smith, J.V., 1977. The MARID (mica-amphibole-rutile-ilmenite-diopside) suite of xenoliths in kimberlite. Geochim. Cosmochim. Acta 41, 309–323.

Day, H.W., 2012. A revised diamond-graphite transition curve. Am. Mineral. 97, 52–62.

de Wit, M.J., 2010. Identification of global diamond metallogenic clusters to assist exploration. In: Proceedings of Diamonds Source to Use, Gaborone, pp. 1–23.

de Wit, M.J., de Ronde, C.E.J., Tredoux, M., Roering, C., Hart, R.J., Armstrong, R.A., Green, R.W., Peberdy, E., Hart, R.A., 1992. Formation of an Archaean continent. Nature 357, 553–562. https://doi.org/10.1038/357553a0.

Dongre, A.N., Tappe, S., 2019. Kimberlite and carbonatite dykes within the Premier diatreme root (Cullinan diamond mine, South Africa): new insights to mineralogical-genetic classifications and magma CO2 degassing. Lithos 338–339, 155–173. https://doi.org/10.1016/j.lithos.2019.04.020.

Donnelly, C.L., Griffin, W.L., Yang, J.H., O'Reilly, S.Y., Li, Q.L., Pearson, N.J., Li, X.H., 2012. In situ U-Pb dating and Sr-Nd isotopic analysis of perovskite: constraints on the age and petrogenesis of the Kuruman Kimberlite Province, Kaapvaal Craton, South Africa. J. Petrol. 53, 2497–2522. https://doi.org/10.1093/petrology/egs057.

Eaton, D.W., Darbyshire, F., Evans, R.L., Grütter, H.S., Jones, A.G., Yuan, X., 2009. The elusive lithosphere–asthenosphere boundary (LAB) beneath cratons. Lithos 109, 1–22.

Erlank, A.J., Waters, F.G., Hawkesworth, C.J., Haggerty, S.E., Allsopp, H.L., Rickard, R. S., Menzies, M., 1987. Evidence for mantle metasomatism in peridotite nodules from the Kimberley pipes, South Africa. In: Mantle Metasomatism. Academic Press, New York, pp. 221–311.

Fitzpayne, A., Giuliani, A., Magalhaes, N., Soltys, A., Fiorentini, M.L., Farquhar, J., 2021. Sulfur isotope constraints on the petrogenesis of the Kimberley kimberlites. Geochem. Geophys. Geosyst. 22. https://doi.org/10.1029/2021GC009845 e2021GC009845.

Foley, S.F., 2011. A reappraisal of redox melting in the Earth's mantle as a function of tectonic setting and time. J. Petrol. 52, 1363–1391.

Fraser, K.J., Hawkesworth, C.J., 1992. The petrogenesis of group 2 ultrapotassic kimberlites from Finsch mine, South Africa. Lithos 28, 327–345. https://doi.org/10.1016/0024-4937(92)90013-O.

Fux, M., Schmidt, M.W., Liebske, C., 2025. Redox melting of garnet lherzolite: generation of carbonated silicate and sulfide melts and implications for OIB formation from chalcophile and redox sensitive elements. Geochem. Geophys. Geosyst. 26. https://doi.org/10.1029/2024GC012025 e2024GC012025.

Gao, S., Harwood, B.P., Metcalf, M.N.G., Dean, B.Y., Campbell, K.M., McFadden, S.I., Flemming, R.L., 2025. Deciphering garnet compositional trends and deformation from a structural-chemical perspective. Mineral. Petrol. 119, 559–581. https://doi.org/10.1007/s00710-025-00921-5.

Gaul, O.F., Griffin, W.L., O'Reilly, S.Y., Pearson, N.J., 2000. Mapping olivine composition in the lithospheric mantle. Earth Planet. Sci. Lett. 182 (3–4), 223–235. https://doi.org/10.1016/S0012-821×(00)00243-0.

Gibson, S.A., 2017. On the nature and origin of garnet in highly-refractory Archean lithospheric mantle: constraints from garnet exsolved in Kaapvaal craton orthopyroxenes. Mineral. Mag. 81, 781–809.

Girnis, A.V., Bulatov, V.K., Brey, G.P., Gerdes, A., Höfer, H.E., 2013. Trace element partitioning between mantle minerals and silico-carbonate melts at 6–12 GPa and applications to mantle metasomatism and kimberlite genesis. Lithos 160–161, 183–200.

Giuliani, A., Phillips, D., Kamenetsky, V.S., Fiorentini, M.L., Farquhar, J., Kendrick, M.A., 2014. Stable isotope (C, O, S) compositions of volatile-rich minerals in kimberlites: a review. Chem. Geol. 374–375, 61–83.

Giuliani, A., Fiorentini, M.L., Martin, L.A.J., Farquhar, J., Phillips, D., Griffin, W.L., LaFlamme, C., 2016. Sulfur isotope composition of metasomatised mantle xenoliths from the Bultfontein kimberlite (Kimberley, South Africa): contribution from subducted sediments and the effect of sulfide alteration on S isotope systematics. Earth Planet. Sci. Lett. 445, 114–124.

Giuliani, A., Pearson, D.G., Soltys, A., Dalton, H., Phillips, D., Foley, S.F., Lim, E., Goemann, K., Griffin, W.L., Mitchell, R.H., 2020. Kimberlite genesis from a common carbonate-rich primary melt modified by lithospheric mantle assimilation. Sci. Adv. 6, eaaz0424. https://doi.org/10.1126/sciadv.aaz0424.

Gréaux, S., Yamada, A., 2019. Density variations of Cr-rich garnets in the upper mantle inferred from the elasticity of uvarovite garnet. Compt. Rendus Geosci. 351, 95–103. https://doi.org/10.1016/j.crte.2018.09.012.

Grew, E.S., Locock, A.J., Mills, S.J., Galuskina, I.O., Galuskin, E.V., Halenius, U., 2013. Nomenclature of the garnet supergroup. Am. Mineral. 98, 785–811.

Griffin, W.L., Cousens, D.R., Ryan, C.G., Sic, S.H., Suter, G.F., 1989. Ni in chrome garnet: a new geothermometer. Contrib. Mineral. Petrol. 103, 199–202. https://doi.org/10.1007/BF00378505.

Griffin, W.L., Fisher, N.I., Friedman, J., Ryan, C.G., O'Reilly, S.Y., 1999. Cr-pyrope garnets in the lithospheric mantle. I. Compositional systematics and relations to tectonic setting. J. Petrol. 40, 679–704. https://doi.org/10.1093/petroj/40.5.679.

Griffin, W.L., Fisher, N.I., Friedman, J.H., O'Reilly, S.Y., Ryan, C.G., 2002. Cr-pyrope garnets in the lithospheric mantle: II. Compositional populations and their distribution in time and space. Geochem. Geophys. Geosyst. 3, 1073. https://doi.org/10.1029/2002GC000298.

Griffin, W.L., O'Reilly, S.Y., Afonso, J.C., Begg, G.C., 2009. The composition and evolution of lithospheric mantle: a re-evaluation and its tectonic implications. J. Petrol. 50, 1185–1204.

Grove, T.L., Holbig, E.S., Barr, J.A., Till, C.B., Krawczynski, M.J., 2013. Melts of garnet lherzolite: experiments, models and comparison to melts of pyroxenite and carbonated lherzolite. Contrib. Mineral. Petrol. 166, 887–910.

Grütter, H.S., Sweeney, R.J., 2000. Tests and constraints on single grain Cr-pyrope barometer models: some initial results. In: GeoCanada 2000, GAC/MAC Annual Meeting, Calgary.
Grütter, H.S., Gurney, J.J., Menzies, A.H., Winter, F., 2004. An updated classification scheme for mantle-derived garnet, for use by diamond explorers. Lithos 77, 841–857.
Grütter, H., Latti, D., Menzies, A., 2006. Cr-saturation arrays in concentrate garnet compositions from kimberlite and their use in mantle barometry. J. Petrol. 47, 801–820.
Gurney, J.J., Moore, R.O., Otter, M.L., Kirkley, M.B., Hops, J.J., McCandless, T.E., 1991. Southern African kimberlites and their xenoliths. In: Magmatism in Extensional Structural Settings. Springer, Berlin, pp. 495–536.
Gurney, J.J., Helmstaedt, H.H., Richardson, S.H., Shirey, S.B., 2010. Diamonds through time. Econ. Geol. 105, 689–712.
Hasterok, D., Chapman, D.S., 2011. Heat production and geotherms for the continental lithosphere. Earth Planet. Sci. Lett. 307, 59–70.
Hoal, K.E.O., Hoal, B.G., Erlank, A.J., Shimizu, N., 1994. Metasomatism of the mantle lithosphere recorded by rare earth elements in garnets. Earth Planet. Sci. Lett. 126, 303–313.
Howarth, G.H., 2026. Kimberlites and olivine lamproites of the Kalahari Craton and related diamond deposits. S. Afr. J. Geol. 129 (1), 301–322. https://doi.org/10.25131/sajg.129.2740.
Huang, J., Huang, F., Evans, L., Glasauer, S., 2015. Vanadium: global (bio)geochemistry. Chem. Geol. 417, 68–89. https://doi.org/10.1016/j.chemgeo.2015.09.019.
Ionov, D.A., Hoefs, J., Harmon, R., 2024. The stable isotope character of the Earth's mantle - a review. Chem. Geol. 670, 122444. https://doi.org/10.1016/j.chemgeo.2024.122444.
Ivanic, T.J., Harte, B., Gurney, J.J., 2012. Metamorphic re-equilibration and metasomatism of highly chromian, garnet-rich peridotitic xenoliths from South African kimberlites. Contrib. Mineral. Petrol. 164, 505–520. https://doi.org/10.1007/s00410-012-0752-6.
James, D.E., 2007. Crust and lithospheric structure – Natural source portable array studies of the continental lithosphere. In: Dziewonski, A.M., Romanowicz, B.A. (Eds.), Treatise on Geophysics, vol. 1. Elsevier, pp. 513–555.
Kawasaki, T., Motoyoshi, Y., 2016. Ti–in–garnet thermometer for ultrahigh-temperature granulites. J. Mineral. Petrol. Sci. 111 (3), 226–240. https://doi.org/10.2465/jmps.150709.
Keshav, S., Corgne, A., Gudfinnsson, G.H., Bizimis, M., McDonough, W.F., Fei, Y., 2005. Kimberlite petrogenesis: insights from clinopyroxene-melt partitioning experiments at 6 GPa in the CaO-MgO-Al2O3-SiO2-CO2 system. Geochim. Cosmochim. Acta 69, 2829–2845.
Keshav, S., Corgne, A., Gudfinnsson, G.H., Fei, Y., 2020. Major and trace element partitioning between majoritic garnet, clinopyroxene, and carbon dioxide-rich liquid in model carbonated peridotite at 10 GPa and interpretations of the element chemistry of majoritic garnet inclusions in diamonds from the subcontinental mantle of Brazil and Guinea. Lithos 362–363, 105486. https://doi.org/10.1016/j.lithos.2020.105486.
Kröner, A., Hoffmann, J.E., 2019. The Archaean Geology of the Kaapvaal Craton, Southern Africa. Springer, p. 302.
Lazarov, M., Woodland, A.B., Brey, G.P., 2009. Thermal state and redox conditions of the Kaapvaal mantle: a study of xenoliths from the Finsch mine, South Africa. Lithos 112, 913–923.
Le Roex, A.P., Class, C., 2016. Metasomatic enrichment of Proterozoic mantle south of the Kaapvaal Craton, South Africa: origin of sinusoidal REE patterns in clinopyroxene and garnet. Contrib. Mineral. Petrol. 171, 14. https://doi.org/10.1007/s00410-015-1222-8.
Le Roex, A.P., Bell, D.R., Davis, P., 2003. Petrogenesis of group I kimberlites from Kimberley, South Africa: evidence from bulk-rock geochemistry. J. Petrol. 44, 2261–2286.
Le Roex, A.P., Tinguely, C., Grégoire, M., 2020. Eclogite and garnet pyroxenite xenoliths from kimberlites emplaced along the southern margin of the Kaapvaal craton, Southern Africa: mantle or lower crustal fragments? J. Petrol. 61. https://doi.org/10.1093/petrology/egaa040.
Li, K., Li, L., Pearson, D.G., Stachel, T., 2019. Diamond isotope compositions indicate altered igneous oceanic crust dominates deep carbon recycling. Earth Planet. Sci. Lett. 516, 190–201.
Locock, A.J., 2008. An Excel spreadsheet to recast analyses of garnet into end-member components, and a synopsis of the crystal chemistry of natural silicate garnets. Comput. Geosci. 34, 1769–1780.
Luth, R.W., Canil, D., 1993. Ferric iron in mantle-derived pyroxenes and a new oxybarometer for the mantle. Contrib. Mineral. Petrol. 113, 236–248.
Mattey, D.P., Carr, R.H., Wright, I.P., Pillinger, C.T., 1984. Carbon isotopes in submarine basalts. Earth Planet. Sci. Lett. 70, 196–206.
Mattey, D., Lowry, D., Macpherson, C., 1994. Oxygen isotope composition of mantle peridotite. Earth Planet. Sci. Lett. 128, 231–241.
McDonough, W.F., Sun, S.S., 1995. The composition of the earth. Chem. Geol. 120, 223–253. https://doi.org/10.1016/0009-2541(94)00140-4.
Menzies, A.H., Shirey, S.B., Carlson, R.W., Gurney, J.J., 1998. Re-Os systematics of Newlands peridotite xenoliths: implications for diamond and lithosphere formation. In: 7th International Kimberlite Conference, Cape Town, pp. 579–581.
Mershon, R.B., Navon, O., Harris, J.W., Weiss, Y., 2025. High-density fluids in diamonds from no. 50 Kimberlite Pipe, Wafangdian, China: the connection to kimberlites. Mineral. Petrol. https://doi.org/10.1007/s00710-025-00931-3.
Mitchell, R.H., 1995. Kimberlites, Orangeites and Related Rocks. Plenum Press, New York, p. 410.
Morimoto, N., 1988. Nomenclature of pyroxenes. Mineral. Petrol. 39, 55–76.
Muramatsu, Y., 1983. Geochemical investigations of kimberlites from the Kimberley area, South Africa. Geochem. J. 17, 71–86. https://doi.org/10.2343/geochemj.17.71.
Neave, D.A., Alexander, G., Stewart, A.G., Hartley, M.E., McCammon, C., 2024. Re-evaluating stoichiometric estimates of iron valence in magmatic clinopyroxene crystals. Contrib. Mineral. Petrol. 179, 5. https://doi.org/10.1007/s00410-023-02080-2.
Nimis, P., Taylor, W.R., 2000. Single clinopyroxene thermobarometry for garnet peridotites; part I, calibration and testing of a Cr-in-Cpx barometer and enstatite-in-Cpx thermometer. Contrib. Mineral. Petrol. 139, 541–554. https://doi.org/10.1007/s004100000156.
Nimis, P., Zanetti, A., Dencker, I., Sobolev, N.V., 2009. Major and trace element composition of chromian diopsides from the Zagadochnaya kimberlite (Yakutia, Russia): metasomatic processes, thermobarometry and diamond potential. Lithos 112, 397–412.
Nimis, P., Preston, R., Perritt, S.H., Chinn, I.L., 2020. Diamond's depth distribution systematics. Lithos 376, 105729.
Nimis, P., Zanetti, A., Franz, L., 2024. A revision of the Ni-in-garnet geothermometer with special regard to its pressure dependence. Lithos 468–469, 107513. https://doi.org/10.1016/j.lithos.2024.107513.
Niyazova, S., Kopylova, M., Dyck, B., Benisek, A., Dachs, E., Stefano, A.D., 2021. The assimilation of felsic xenoliths in kimberlites: insights into temperature and volatiles during kimberlite emplacement. Contrib. Mineral. Petrol. 176, 84. https://doi.org/10.1007/s00410-021-01837-x.
Nosova, A.A., Kargin, A.V., Erofeeva, K.G., Dokuchaev, A.Y., Kondrashov, I.A., Okina, O. I., 2025. Garnet and clinopyroxene from 1.98 Ga Kimozero kimberlites, Karelia, Russia: evidence of the multistage evolution of the ancient lithospheric mantle. Lithos 494–495, 107911. https://doi.org/10.1016/j.lithos.2024.107911.
O'Neill, H.S.C., Wood, B.J., 1979. An experimental study of Fe-Mg partitioning between garnet and olivine and its calibration as a geothermometer. Contrib. Mineral. Petrol. 70, 59–70. https://doi.org/10.1007/BF00371872.
Ouyang, D., Bao, H., Byerly, G.R., Li, Q., 2024. Light oxygen isotopic composition in deep mantle reveals oceanic crust subduction before 3.3 billion years ago. Commun. Earth Environ. 5, 34. https://doi.org/10.1038/s43247-023-01197-3.
Pearson, D.G., Woodhead, J., Janney, P.E., 2019. Kimberlites as geochemical probes of earth's mantle. Elements 15, 387–392. https://doi.org/10.2138/gselements.15.6.387.
Pineau, F., Javoy, M., 1983. Carbon isotopes and concentrations in mid-oceanic ridge basalts. Earth Planet. Sci. Lett. 62, 239–257.
Pokhilenko, N.P., Agashev, A.M., Litasov, K.D., Pokhilenko, L.N., 2015. Carbonatite metasomatism of peridotite lithospheric mantle: implications for diamond formation and carbonatite-kimberlite magmatism. Russ. Geol. Geophys. 56, 280–295.
Ramokgaba, L., Le Roex, A.P., Robey, J.V.A., 2021. Phlogopite-rich and phlogopite-poor kimberlite intrusions within the Du Toitspan kimberlite pipe, South Africa: petrogenetic relationships and localised source heterogeneity. Lithos 390–391, 106125. https://doi.org/10.1016/j.lithos.2021.106125.
Robinson, D.N., 1975. Magnetite-serpentine-calcite dykes at Premier Mine and aspects of their relationship to kimberlite and to carbonatite of alkalic carbonatite complexes. Phys. Chem. Earth 9, 61–70. https://doi.org/10.1016/0079-1946(75)90007-5.
Ryan, C.G., Griffin, W.L., Pearson, N.J., 1996. Garnet geotherms: a technique for derivation of P–T data from Cr-pyrope garnets. J. Geophys. Res. 101, 5611–5625. https://doi.org/10.1029/95JB03207.
Sablukova, L.I., Sablukov, S.M., Stegnitsky, Y.B., Karpenko, M.A., 2012. Green garnets of the wehrlite mantle xenoliths from kimberlites: their composition and origin. In: 10th International Kimberlite Conference, Bangalore. https://doi.org/10.29173/ikc3707.
Schulze, D.J., 1989. Green garnets from South African kimberlites and their relationship to wehrlites and crustal uvarovites. Spec. Publ. - Geol. Soc. Aust. 14, 820–826.
Scott-Smith, B.H., Nowicki, T.E., Russell, J.K., Webb, K.J., Mitchell, R.H., Hetman, C.M., Jock, Robey, J.V., 2018. A Glossary of Kimberlite and Related Terms. Scott-Smith Petrology Inc., North Vancouver, BC, Canada.
Simon, N.C.S., Neumann, E.R., Bonadiman, C., Coltorti, M., Delpech, G., Grégoire, M., Widom, E., 2008. Ultra-refractory domains in the oceanic mantle lithosphere sampled as mantle xenoliths at ocean islands. J. Petrol. 49, 1223–1251. https://doi.org/10.1093/petrology/egn023.
Skinner, E.M.W., 1989. Contrasting group I and group II kimberlite petrology: towards a genetic model for kimberlites. Spec. Publ. - Geol. Soc. Aust. 14, 528–544.
Smith, C.B., Allsopp, H.L., Kramers, J.D., Hutchinson, G., Roddick, J.C., 1985. Emplacement ages of Jurassic–Cretaceous South African kimberlites by the Rb–Sr method on phlogopite and whole-rock samples. Trans. Geol. Soc. S. Afr. 88, 249–266.
Sobolev, N.V., Logvinova, A.M., Zedgenizov, D.A., Seryotkin, Y.V., Yefimova, E.S., Floss, C., Taylor, L.A., 2004. Mineral inclusions in microdiamonds and macrodiamonds from kimberlites of Yakutia: a comparative study. Lithos 77, 225–242. https://doi.org/10.1016/j.lithos.2004.04.001.
Sobolev, N.V., Tomilenko, A.A., Bul'bak, T.A., Logvinova, A.M., 2019. Composition of hydrocarbons in diamonds, garnet, and olivine from diamondiferous peridotites from the Udachnaya pipe in Yakutia, Russia. Engineering 5, 471–478.
Stachel, T., Aulbach, S., Harris, J.W., 2022. Mineral inclusions in lithospheric diamonds. Rev. Mineral. Geochem. 88, 307–392.
Stagno, V., Aulbach, S., 2022. Redox heterogeneity of Earth's mantle. Elements 18, 29–34.
Stagno, V., Ojwang, D.O., McCammon, C.A., Frost, D.J., 2013. The oxidation state of the mantle and the extraction of carbon from Earth's interior. Nature 493, 84–88. https://doi.org/10.1038/nature11679.

Stanley, J.R., Flowers, R.M., 2016. Dating kimberlite emplacement with zircon and perovskite (U-Th)/He geochronology. Geochem. Geophys. Geosyst. 17, 4517–4533. https://doi.org/10.1002/2016GC006519.

Sudholz, Z.J., Yaxley, G.M., Jaques, A.L., Brey, G.P., 2021a. Experimental recalibration of the Cr-in-clinopyroxene geobarometer: improved precision and reliability above 4.5 GPa. Contrib. Mineral. Petrol. 176, 11.

Sudholz, Z.J., Yaxley, G.M., Jaques, A.L., Chen, J., 2021b. Ni-in-garnet geothermometry in mantle rocks: a high pressure experimental recalibration between 1100 and 1325°C. Contrib. Mineral. Petrol. 176, 32. https://doi.org/10.1007/s00410-021-01791-8.

Sun, C., Liang, Y., 2014. An assessment of subsolidus re-equilibration on REE distribution among mantle minerals olivine, orthopyroxene, clinopyroxene, and garnet in peridotites. Chem. Geol. 372, 80–91.

Tappe, S., Budde, G., Stracke, A., Wilson, A., Kleine, T., 2020a. The tungsten-182 record of kimberlites above the African superplume: exploring links to the core-mantle boundary. Earth Planet. Sci. Lett. 547, 116473. https://doi.org/10.1016/j.epsl.2020.116473.

Tappe, S., Stracke, A., Van Acken, D., Strauss, H., Luguet, A., 2020b. Origins of kimberlites and carbonatites during continental collision - insights beyond decoupled Nd-Hf isotopes. Earth-Sci. Rev. 208, 103287. https://doi.org/10.1016/j.earscirev.2020.103287.

Tomlinson, E.L., Holland, T.J.B., 2021. Thermodynamic model for the subsolidus evolution and melting of peridotite. J. Petrol. 62, 1–23. https://doi.org/10.1093/petrology/egab012.

Vernières, J., Godard, M., Bodinier, J.L., 1997. A plate model for the simulation of trace elements during partial melting and magma transport in the Earth's upper mantle. J. Geophys. Res. 102, 24771–24784.

Walsh, C., Kamber, B.S., Tomlinson, E.L., 2023. Deep, ultra-hot-melting residues as cradles of mantle diamond. Nature 615, 450–454. https://doi.org/10.1038/s41586-022-05665-2.

Waters, F.G., Erlank, A.J., Daniels, L.R.M., 1989. Contact relationships between metasomatised peridotite in a MARID rock and kimberlite xenolith. Geochem. J. 23, 11–17.

Weiss, Y., Griffin, W.L., Navon, O., 2013. Diamond-forming fluids in fibrous diamonds: the trace-element perspective. Earth Planet. Sci. Lett. 376, 110–125.

White, J.L., Sparks, R.S.J., Bailey, K., Barnett, W.P., Field, M., Windsor, L., 2012. Kimberlite sills and dykes associated with the Wesselton kimberlite pipe, Kimberley, South Africa. S. Afr. J. Geol. 115, 1–32. https://doi.org/10.2113/gssajg.115.1.1.

Woodland, A.B., Uenver-Thiele, L., Seitz, H.M., 2018. Influence of metasomatism on vanadium-based redox proxies for mantle peridotite. Geochem. Persp. Lett. 8, 11–16. https://doi.org/10.7185/geochemlet.1822.

Wu, F.Y., Mitchell, R.H., Li, Q.L., Sun, J., Liu, C.Z., Yang, Y.H., 2013. In situ U-Pb age determination and Sr-Nd isotopic analysis of perovskite from the Premier (Cullinan) kimberlite, South Africa. Chem. Geol. 353, 83–95. https://doi.org/10.1016/j.chemgeo.2012.06.002.

Zhong, X., Andersen, N.H., Dabrowski, M., Jamtveit, B., 2019. Zircon and quartz inclusions in garnet used for complementary Raman thermobarometry: application to the Holsnøy eclogite, Bergen Arcs, Western Norway. Contrib. Mineral. Petrol. 174, 50. https://doi.org/10.1007/s00410-019-1584-4.